

SOURCE-FREE TEST-TIME ADAPTATION FOR DIFFUSION-BASED VIRTUAL TRY-ON

Anonymous authors

Paper under double-blind review

ABSTRACT

The rapid growth of e-commerce has driven notable advancements in diffusion-based virtual try-on models. Virtual try-on models, however, suffer significant quality degradation when deployed on real-world data that differs from their source (training) distribution. To address challenges in quality degradation due to domain shifts, we introduce a test-time adaptation framework that enhances try-on quality during diffusion denoising (inference time) without requiring model retraining or updates to the original network parameters. We introduce statistical distribution matching across complementary domains during the diffusion denoising process. Comprehensive evaluation across four state-of-the-art diffusion models (IDM-VTON, LaDI-VTON, Stable-VTON, TPD) and three datasets (VITON-HD, DressCode, DeepFashion) demonstrates notable improvements across multiple dataset-method combinations, with sharpness gains averaging 7.74% and distortion reduction of 0.95%. Our approach addresses important practical challenges in commercial virtual try-on deployment, enabling quality improvements across diverse domain conditions while preserving the original model’s capabilities.

1 INTRODUCTION

Virtual try-on is a key application in e-commerce, enabling users to digitally wear garments or visualize them on template models. Over the years, advancements in try-on technology have focused on efficiently “warping” garments onto a target person while preserving intricate details. Early machine learning-based approaches Han et al. (2018); He et al. (2022); Wang et al. (2018) achieved some success in detail retention but were limited by low resolution and common artifacts such as blurring, color bleeding, and texture inconsistencies.

Appearance flow-based methods Zhou et al. (2016); Shim et al. (2024); Gou et al. (2023); Yu et al. (2023); Chen et al. (2023b) have treated virtual try-on as a view synthesis problem, while 3D geometric formulations Zhao et al. (2021) attempt to map input image pixels to their expected positions in the warped garment. However, these methods often struggle with generalization, as models trained on one dataset frequently fail when applied to unseen data. Hybrid approaches, such as DCI-VTON Gou et al. (2023), integrate appearance flow with diffusion models, yet they still exhibit distortions when handling new garment types or poses.

Denoising diffusion probabilistic models (DDPMs) have shown strong performance in image-to-image tasks such as segmentation, object detection, and virtual try-on Tian et al. (2023); Chen et al. (2023a); Gou et al. (2023); Kim et al. (2024); Zhu et al. (2023). These models are typically conditioned on input images and garments, sometimes using text for finer control Gou et al. (2023). While they preserve texture well Yang et al. (2024) and generalize across domains, they struggle with unseen garment styles and poses due to their stochastic nature. To address domain shifts in virtual try-on, we propose the first test-time adaptation (TTA) framework for diffusion models that refines generation during inference without modifying model parameters. Unlike prior methods that require retraining Xing et al. (2024), our approach is source-free and adapts per image. While TTA has seen use in classification Wang et al. (2021); Boudiaf et al. (2022); Niu et al. (2022); Osowiechi et al. (2024), its potential for image-to-image tasks remains largely unexplored.

Our method refines denoised outputs across multiple diffusion steps using a novel multi-domain statistical loss comprising: (1) Image Domain Consistency – Aligning pixel intensity distributions for accurate color and illumination, (2) Frequency Domain Consistency – Preserving garment details

using Discrete Cosine Transform (DCT), and (3) Local Structural Consistency – Maintaining spatial coherence through local distribution matching. Our approach is ‘training-free’ as it does not modify the parameters (Θ) of the pretrained diffusion model. It operates as a plug-and-play guidance mechanism during inference, preserving the original model’s integrity while adapting its output to new data. Our key contributions are: (1) A novel guidance mechanism that adapts diffusion denoising through statistical distribution matching without modifying network parameters or requiring source training data, (2) Three complementary loss functions operating across image, frequency, and local structure domains, with theoretical convergence guarantees for the optimization process, (3) Comprehensive evaluation demonstrating consistent improvements across four state-of-the-art models and three datasets, with notable gains in semantic consistency (up to 4.2% CLIP improvement) and visual sharpness (up to 56.8% enhancement).

2 RELATED WORK

2.1 VIRTUAL TRY-ON

Virtual try-on has evolved significantly from early coarse-to-fine pipelines such as VITON Han et al. (2018), which combined warping and refinement modules to mitigate blurry artifacts. CP-VTON Wang et al. (2018) introduced geometric matching and thin-plate spline transformations for better garment alignment, while style-based frameworks like StyleGAN-VITON He et al. (2022) incorporated local context to improve realism and texture consistency. Subsequent work addressed scalability and resolution challenges. Outfit-VTON Neuberger et al. (2020) enabled multi-garment try-on with compositional architecture, while VITON-HD Choi et al. (2021) and HR-VTON Lee et al. (2022) pushed towards high-resolution synthesis (1024×768), employing segmentation-guided metrics and joint learning of warping and parsing for improved realism in occluded regions. However, many of these methods remain sensitive to domain shifts in pose, lighting, and garment styles, struggling with generalization when applied to unseen data distributions.

2.2 DIFFUSION MODELS FOR VIRTUAL TRY-ON

Denoising Diffusion Probabilistic Models (DDPMs) Ho et al. (2020) have recently emerged as powerful generative frameworks, achieving high-fidelity generation under complex conditions. Stable Diffusion Rombach et al. (2022) demonstrated remarkable generalization capabilities via text conditioning and fine-tuning approaches. In virtual try-on, diffusion-based models such as DCI-VTON Gou et al. (2023), LaDI-VTON Morelli et al. (2023), TPD Yang et al. (2024), and TryOnDiff Zhu et al. (2023) produce high-resolution results using both paired and unpaired training data. While they preserve texture well Yang et al. (2024) and show improved generalization compared to earlier methods, they often fail to preserve fine-grained details such as logos, textures, and garment boundaries under domain shifts, frequently introducing hallucinated artifacts beyond the clothing region. CAT-DM Zeng et al. (2024) integrates ControlNet for enhanced conditioning but relies on parameter updates during inference, increasing computational cost and requiring access to source training data.

2.3 TEST-TIME ADAPTATION

Test-time adaptation aims to bridge domain gaps by adapting models using unlabeled test data without access to source training data. Entropy minimization methods such as TENT Wang et al. (2021) update batch normalization statistics to align distributions, while parameter-



Figure 1: TTA enhances image quality by preserving garment details (top), patterns (middle), and object shapes/positions (bottom).

free methods like LAME Boudiaf et al. (2022) and EATA Niu et al. (2022) preserve source model integrity by filtering uncertain samples and avoiding parameter modifications. Recent works explore single-image adaptation scenarios. SITA Khurana et al. (2021) applies entropy-based consistency across class-preserving augmentations, while S-ITTA Janouskova et al. adapts segmentation masks in zero-shot settings. However, these approaches are fundamentally designed for classification and segmentation tasks, relying on discrete predictions, categorical entropy, and batch normalization statistics that are absent in generative diffusion models. However, these approaches are fundamentally incompatible with generative diffusion models due to key architectural and objective mismatches: (1) classification TTA relies on discrete class predictions and categorical entropy, while diffusion operates in continuous latent spaces; (2) existing methods depend on batch normalization updates, but diffusion models use layer/group normalization; (3) classification TTA leverages prediction confidence as pseudo-supervision, which is unavailable in image generation tasks. To our knowledge, this is the first TTA method for diffusion-based image-to-image generation. We propose a source-free framework using statistical distribution matching during denoising, avoiding the discrete prediction dependencies of traditional TTA methods.

3 PROPOSED METHODOLOGY

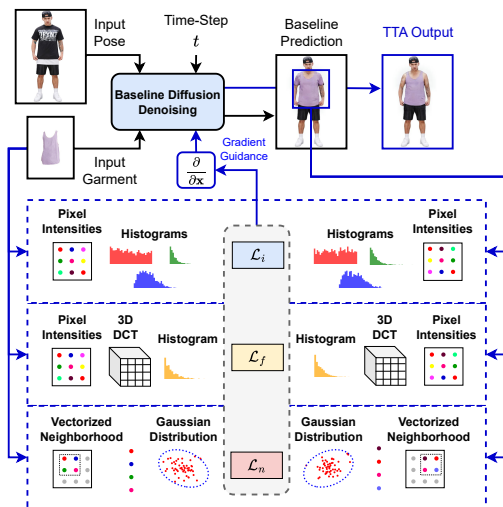


Figure 3: Overview of the proposed TTA framework. Blue arrows denote TTA guidance, black arrows denote zero-shot prediction. Guidance losses \mathcal{L}_i , \mathcal{L}_f , and \mathcal{L}_n refine predictions during denoising, enabling plug-and-play TTA.



Figure 2: Illustration of domain shift in virtual try-on: Aligned domains (top) yield clear garment details, while shifts in lighting or style (bottom) cause blurred textures and distorted patterns.

We propose a source-free TTA framework to improve virtual try-on quality (Fig. 3), addressing domain shift failures such as illegible text and distorted stripe patterns (Fig. 2). Domain shifts hinder e-commerce deployment and user experience. Our method mitigates this by guiding diffusion with statistical matching of color, texture, and structure to preserve garment fidelity across domains.

3.1 GUIDED DENOISING DIFFUSION

DDPMs Ho et al. (2020) are a recent class of generative models that have shown tremendous success in tasks such as conditional generation, inpainting, and translation. The ability of DDPMs to generalize well stems from learning a first-order Markov process from Gaussian noise to structured outputs. Given an input image \mathbf{x}_0 , noise is progressively added through a fixed Markov process for T time-steps until \mathbf{x}_T is distributed as a standard Gaussian $\mathcal{N}(\mathbf{0}, \mathbf{I})$. In other words, a sequence of data $\{\mathbf{x}_i\}$, $i = 0, 1, \dots, T$ is sampled with Gaussian noise with variance $\beta_t \in (0, 1)$ at time-step t during the forward process as

$$q(\mathbf{x}_t | \mathbf{x}_0) = \sqrt{\bar{\alpha}_t} \mathbf{x}_0 + \sqrt{1 - \bar{\alpha}_t} \epsilon \quad (1)$$

where $\epsilon \sim \mathcal{N}(\mathbf{0}, \mathbf{I})$ is the noise added to the input, $\bar{\alpha}_t = \prod_{j=1}^t \alpha_j$, and $\alpha_t = 1 - \beta_t$ for $t = 1, 2, \dots, T$ is the noise scheduling parameter. The distributions of the forward process are denoted

162 by $q(\mathbf{x}_t | \mathbf{x}_{t-1})$, which are assumed to follow a first-order Markov process. The reverse (or denoising
163 process) is modeled using a parametric family of distributions denoted as $p_\theta(\mathbf{x}_{t-1} | \mathbf{x}_t)$.
164

165 The idea is that the distribution of \mathbf{x}_T can be approximated reasonably well by the standard Gaussian
166 distribution i.e., $q(\mathbf{x}_T) \sim \mathcal{N}(\mathbf{0}, \mathbf{I})$. The goal of the DDPM is to estimate the parameters of p_θ by
167 optimizing a variational lower bound on the data likelihood \mathbf{x}_0 under the model p_θ . The loss function
168 optimized by the DDPM at a time-step t is as follows:

$$169 \quad L_t = \mathbb{E}_{\mathbf{x}_0, \epsilon} [\|\epsilon - \epsilon_\theta(\mathbf{x}_t, t)\|^2], \quad (2)$$

171 where ϵ and $\epsilon_\theta(\mathbf{x}_t, t)$ correspond to the input (real) noise and the predicted noise at time step t ,
172 respectively. The denoised image at any time step t is given by
173

$$174 \quad \mathbf{x}_{t-1} = \frac{1}{\sqrt{\alpha_t}} \left(\mathbf{x}_t - \frac{1 - \alpha_t}{\sqrt{1 - \bar{\alpha}_t}} \epsilon_\theta(\mathbf{x}_t, t) \right) + \sigma_t \epsilon, \quad (3)$$

176 where σ_t is the variance of the noise and the goal is to bring the distribution of \mathbf{x}_0 as close as possible
177 to that of source domain data. However, the aforementioned relation makes the reverse process slow
178 due to the requirement of all past denoising outputs to compute a single output. To speed up the
179 reverse process, DDIM Song et al. (2020) sampling was introduced, where multiple time-steps can
180 be skipped and the denoised outputs can still be computed in an efficient manner. To this end, the
181 DDIM sampling process is described as
182

$$183 \quad \mathbf{x}_{t-1}^g = \sqrt{\bar{\alpha}_{t-1}} (\mathbf{x}_t^g - \mathbf{x}_{0,t}^g) + (1 - \bar{\alpha}_{t-1} - \sigma_t^2 \epsilon_\theta(\mathbf{x}_t^g, t)) + \sigma_t \epsilon, \quad (4)$$

184 where the term $\mathbf{x}_{0,t}^g$ is the predicted denoised image for \mathbf{x}_0^g conditioned on \mathbf{x}_t and is expressed as
185

$$186 \quad \mathbf{x}_{0,t}^g = \frac{\mathbf{x}_t^g - \sqrt{1 - \bar{\alpha}_t} \epsilon_\theta(\mathbf{x}_t^g, t)}{\sqrt{\bar{\alpha}_t}}. \quad (5)$$

188 In order to provide guidance to the denoising process, a generalized TTA algorithm called GDA
189 Tsai et al. (2024) was proposed to update the denoised outputs at each time-step to improve the
190 generations. An update is performed using the gradient of a suitable objective function $\mathcal{L}(\mathbf{x})$ by first
191 sampling from the reverse process as $\hat{\mathbf{x}}_{t-1}^g \sim p_\theta(\mathbf{x}_{t-1}^g | \mathbf{x}_t^g)$ and updating this sample as
192

$$193 \quad \mathbf{x}_{t-1}^g = \hat{\mathbf{x}}_{t-1}^g - \alpha \nabla_{\mathbf{x}} \mathcal{L}(\mathbf{x})_{\{\mathbf{x}=\mathbf{x}_{0,t}^g, \mathbf{x}_0\}}, \quad (6)$$

195 where the inputs to the loss objective are $\mathbf{x}_{0,t}^g$ and \mathbf{x}_0 , and α is a learning-rate hyperparameter.
196 Through this guidance, the denoised outputs are tuned to exhibit better structure and consequently,
197 visually better generations. In the context of virtual try-on, we propose to guide the denoising using
198 a loss objective that improves the color, local structure, and textures in the generated outputs. The
199 loss function is described in the section below.
200

201 3.2 TEST-TIME OPTIMIZATION OBJECTIVE

202 In real-world scenarios, the absence of ground-truth references and misalignment between input
203 and generated garments hinder the reliability of full-reference metrics. Moreover, diffusion models
204 trained on a single distribution often fail to generalize across diverse garment types. To overcome
205 these challenges, we introduce distribution-level guidance at inference using three statistical losses,
206 each designed to preserve a specific aspect of garment fidelity and fine detail.
207

208 **Image-Space Distribution Loss:** The input and the generated garment are expected to have similar
209 distribution of colors and textures in order to observe visually coherent try-on renderings. In this
210 regard, we propose matching the distribution of pixel intensities within the garment regions between
211 the input and output. Since the regions of a person outside the garment need not be modified, we
212 first mask out the garment regions in the input and output and collect the pixel intensities into three
213 dimensional vectors, where each dimension corresponds to R, G and B channels. Let the input
214 garment image be denoted as \mathbf{x} and the generated image as $\hat{\mathbf{y}}$. Let the binary masks corresponding
215 to the input and generated garments be \mathbf{m}_x and \mathbf{m}_g , respectively. The set of coefficients of the
input and output can be obtained as $\mathcal{X} = \{\mathbf{x}_{i,j} : \mathbf{m}_x(i, j) = 1\}$ and $\mathcal{Y} = \{\hat{\mathbf{y}}_{i,j} : \mathbf{m}_g(i, j) = 1\}$

respectively, where (i, j) correspond to the pixel locations. Using the coefficients, we construct two sets of channel-wise histograms $h(\mathcal{X}, N_b)$ and $h(\mathcal{Y}, N_b)$, where N_b is the number of bins in the histogram and a hyperparameter. The objective is to minimize the L1-loss between the two histograms as

$$\mathcal{L}_i^c = \frac{1}{N_b} \sum_{j=1}^{N_b} |h_j^c(\mathcal{X}, N_b) - h_j^c(\mathcal{Y}, N_b)|, \quad (7)$$

where $h_j(\cdot)$ refers to the j^{th} bin, and c refers to the color channel. Here, we approximate the distributions of \mathcal{X} and \mathcal{Y} using histograms, since we do not make any assumptions on the form of each distribution. Although we considered a Gaussian approximation of the pixel intensity vectors, the histograms of garments were observed to neither follow a Gaussian nor any known distribution. The losses are averaged across the channels to calculate the loss in the image space \mathcal{L}_i as $\mathcal{L}_i = \frac{1}{3} \sum_c \mathcal{L}_i^c$. The mask m_x is provided by cloth masks from the dataset or generated using the SAM segmentation model Kirillov et al. (2023), while m_g is obtained from an intermediate prediction of a baseline model. During try-on generation, most models implicitly create a garment mask to constrain garment warping, which we leverage in our approach.

Frequency-Domain Distribution Loss: To preserve frequency information (such as edges and corners) along with spatial details in garments, we match the distributions of the discrete cosine transform (DCT) coefficients between the input and output garment regions. The DCT coefficients capture high-frequency details like periodic stripes and checkered textures. Similarly to the previous image domain histograms, we match the distance L1 between DCT histograms. Here, we compute a bounding box around the input and generated garments, applying a non-overlapping 3D-DCT within these boxes. Specifically, we perform a 2D-DCT on $K \times K$ spatial blocks, then a 1D-DCT along channels. The resulting 3D block of dimension $3 \times K \times K$ is flattened to a vector for histogram computation. The coefficients are obtained as $\mathcal{S}_i = \{\text{DCT-1D}(\text{DCT-2D}(\mathbf{x}_b, K))\}$ and $\mathcal{S}_g = \{\text{DCT-1D}(\text{DCT-2D}(\hat{\mathbf{y}}_b, K))\}$, where \mathbf{x}_b and $\hat{\mathbf{y}}_b$ correspond to the regions of the bounding box (garment) in \mathbf{x} and $\hat{\mathbf{y}}$. In this case we obtain histograms $h(\mathcal{S}_i, N_b)$ and $h(\mathcal{S}_g, N_b)$ and compute the L1-loss between them to obtain our frequency-domain loss as

$$\mathcal{L}_f = \frac{1}{N_b} \sum_{j=1}^{N_b} |h_j(\mathcal{S}_i, N_b) - h_j(\mathcal{S}_g, N_b)|. \quad (8)$$

When 2D blocks extend beyond the bounding box, any extra pixels are discarded. This loss in the frequency domain helps to preserve texture details and adds sharpness to the generated images. Choosing an appropriate block size is important. If K is too small, it may not capture many high-frequency details, and a high value of K would result in increased computation times.

Local-Structure Distribution Loss: While the previous losses target global distribution matching, preserving local and fine-grained garment structures is essential. To achieve this, we introduce a loss that aligns the distribution of spatial intensities within a pixel’s neighborhood. Specifically, for each color channel, we flatten the surrounding pixel intensities into a d -dimensional vector and collect these vectors from garment regions in both input and output images. We then compute the sample means (μ_i, μ_g) and covariance matrices (Σ_i, Σ_g) for the input and generated garments. Assuming these vectors follow Gaussian distributions, we calculate the KL-divergence between them. Unlike the other two losses, this Gaussian assumption was observed to hold reasonably well for these vectors. The loss between the input and garment neighborhood distributions is computed as

$$\mathcal{L}_n = \frac{1}{2} \left(\text{tr} (\Sigma_g^{-1} \Sigma_i) + (\mu_g - \mu_i)^\top \Sigma_g^{-1} (\mu_g - \mu_i) - d + \ln \frac{\det \Sigma_g}{\det \Sigma_i} \right). \quad (9)$$

This loss effectively captures fine structures that the other two losses might miss. By using non-overlapping neighborhoods within garment regions, we reduce feature redundancy. Here, the neighborhood size affects the amount of local information that needs to be modeled. A large neighborhood vector dimension d could result in the loss of local structural information. Hence, we use a small value of $d = 4$ (2×2 neighborhood) for all our experiments.



Figure 4: Qualitative comparison showing TTA improvements: (a) enhanced stripe regularity (IDM-VTON), (b) improved color accuracy (Stable-VITON), (c) better pattern preservation (TPD), and (d) consistent garment color generation (LaDI-VTON).

Algorithm 1 Test-Time Adaptation for Virtual Try-On

Require: Person image I_p , garment image I_g , pre-trained diffusion model θ
Require: Hyperparameters $\lambda_1, \lambda_2, \lambda_3$, learning rate α
Ensure: Enhanced try-on output x_0^{TTA}

- 1: Extract garment masks m_x, m_g from I_g and initial prediction
- 2: Initialize noisy latent $x_T \sim \mathcal{N}(0, I)$
- 3: **for** $t = T, T-1, \dots, 1$ **do**
- 4: Sample $\hat{x}_{t-1}^g \sim p_\theta(x_{t-1}^g | x_t^g)$ {Baseline denoising step}
- 5: Compute predicted clean image: $x_{0,t}^g = \frac{x_t^g - \sqrt{1-\bar{\alpha}_t} \epsilon_\theta(x_t^g, t)}{\sqrt{\bar{\alpha}_t}}$
- 6: **Compute Statistical Losses:**
- 7: $\mathcal{L}_i = \frac{1}{3} \sum_{c=1}^3 \frac{1}{N_b} \sum_{j=1}^{N_b} |h_j^c(\mathcal{X}, N_b) - h_j^c(\mathcal{Y}, N_b)|$ {Image histogram}
- 8: $\mathcal{L}_f = \frac{1}{N_b} \sum_{j=1}^{N_b} |h_j(\mathcal{S}_i, N_b) - h_j(\mathcal{S}_g, N_b)|$ {DCT histogram}
- 9: $\mathcal{L}_n = \frac{1}{2} [\text{tr}(\Sigma_g^{-1} \Sigma_i) + (\mu_g - \mu_i)^T \Sigma_g^{-1} (\mu_g - \mu_i) - d + \ln \frac{\det \Sigma_g}{\det \Sigma_i}]$ {KL divergence}
- 10: $\mathcal{L} = \lambda_1 \mathcal{L}_i + \lambda_2 \mathcal{L}_f + \lambda_3 \mathcal{L}_n$
- 11: **Apply Guidance:**
- 12: $x_{t-1}^g = \hat{x}_{t-1}^g - \alpha \nabla_{x_{0,t}^g} \mathcal{L}(x_{0,t}^g, I_g)$ {Gradient-based update}
- 13: **end for**
- 14: **return** $x_0^{TTA} = x_0^g$

304
 305 **3.3 OVERALL OBJECTIVE FUNCTION**

306
 307 The three losses are combined into a single objective that is expected to preserve global colors,
 308 structural details in textured regions, as well as local fine-grained structural information. The overall
 309 loss \mathcal{L} is

$$\mathcal{L} = \lambda_1 \mathcal{L}_i + \lambda_2 \mathcal{L}_f + \lambda_3 \mathcal{L}_n, \quad (10)$$

310 where $\lambda_1, \lambda_2, \lambda_3$ are hyperparameters chosen in a manner such that the losses are on a similar scale.
 311 Importantly, the λ values are hyperparameters for our external guidance mechanism, not the dif-
 312 fusion model, which remains frozen. Instead of fine-tuning, we guide the denoising process by
 313 optimizing the output at each step using Equation equation 6. Our three-part loss targets comple-
 314 mentary aspects of garment fidelity: (1) \mathcal{L}_i enforces global consistency via histogram matching,
 315 (2) \mathcal{L}_f preserves high-frequency details using DCT alignment, and (3) \mathcal{L}_n maintains local structure
 316 through neighborhood distribution matching.

317
 318 **Convergence Analysis:** We provide theoretical convergence guarantees (proof in Appendix B) for
 319 our guidance process, summarized in the following theorem:

320
 321 **Theorem 3.1** (Convergence Guarantee). *Assume the combined loss function $\mathcal{L}(\mathbf{x}_{0,t}^g, \mathbf{x}_0)$ is L -
 322 smooth. Then for learning rate $\alpha \leq \frac{1}{L}$, the guidance process satisfies:*

$$323 \quad \mathcal{L}(\mathbf{x}_{t+1}^g, \mathbf{x}_0) \leq \mathcal{L}(\mathbf{x}_t^g, \mathbf{x}_0) - \frac{\alpha}{2} \|\nabla \mathcal{L}(\mathbf{x}_t^g, \mathbf{x}_0)\|^2$$

Dataset	Method	Sharpness \uparrow		Distortion \downarrow		TP \uparrow		PC \uparrow		CLIP \uparrow	
		Baseline	TTA	Baseline	TTA	Baseline	TTA	Baseline	TTA	Baseline	TTA
VITON-HD	IDM-VTON	0.493	0.773	0.045	0.033	0.716	0.721	0.809	0.833	0.837	0.848
	LaDI-VTON	0.521	0.542	0.043	0.045	0.735	0.734	0.843	0.844	0.858	0.858
	Stable-VTON	0.425	0.427	0.039	0.039	0.763	0.784	0.847	0.858	0.840	0.845
	TPD	0.457	0.463	0.044	0.042	0.760	0.759	0.845	0.864	0.856	0.856
DressCode	IDM-VTON	0.384	0.398	0.055	0.053	0.634	0.645	0.801	0.805	0.747	0.750
	LaDI-VTON	0.505	0.511	0.051	0.049	0.686	0.689	0.817	0.811	0.769	0.775
	Stable-VTON	0.477	0.486	0.043	0.043	0.676	0.692	0.818	0.818	0.770	0.771
	TPD	0.328	0.342	0.062	0.054	0.668	0.699	0.793	0.800	0.763	0.764
Average Improvement		7.74%		0.95%		1.77%		1.09%		1.24%	

Table 1: Quantitative Results. The metrics used are sharpness, distortion, texture preservation (TP), pattern consistency (PC) and CLIP consistency.

and converges to a stationary point with rate:

$$\min_{0 \leq k \leq T} \|\nabla \mathcal{L}(\mathbf{x}_{0,k}^g, \mathbf{x}_0)\|^2 \leq \frac{2L(\mathcal{L}(\mathbf{x}_{0,0}^g, \mathbf{x}_0) - \mathcal{L}^*)}{T} \quad (11)$$

4 EXPERIMENTS AND RESULTS

Experimental Setup: All experiments were run on three NVIDIA RTX 3090 GPUs (24GB VRAM each). Garment masks are obtained from dataset annotations when available, or generated using SAM Kirillov et al. (2023) for robustness across datasets. We use DDIM sampling with 30 timesteps and apply guidance at each denoising step. Hyperparameters are selected such that all three loss components are in a similar scale, with $\lambda_2 = 1000$ held constant across methods while λ_1 and λ_3 are method-specific. All experiments use identical random seeds for fair comparison. The following parameters are kept consistent: DCT block size $K = 32$, neighborhood dimension $d = 4$ (2×2 regions), 100 bins for image-space and 250 for the frequency-domain histograms, and the learning rate is set to $\alpha = 1.0$.

Datasets and Evaluation Protocol: We evaluate on three datasets with complementary characteristics: VITON-HD (2,032 test pairs, high-resolution controlled conditions), DressCode (1,800 pairs, diverse poses and garment types), and DeepFashion (146 carefully curated pairs with challenging real-world conditions). While DeepFashion has fewer samples, we supplement quantitative analysis with extensive qualitative evaluations to ensure a complete evaluation.

Statistical Significance: Beyond mean improvements, we analyze effect sizes using Cohen’s d to assess practical significance. Our method achieves medium-to-large effect sizes for key metrics: sharpness improvement shows $d=0.51\text{-}0.70$ for IDM-VTON and LaDI-VTON, while distortion reduction demonstrates $d=0.48\text{-}0.78$ across methods.

Evaluation Metrics: Traditional metrics like SSIM, LPIPS, and FID are ill-suited for unpaired virtual try-on, as they rely on pixel-level correspondence, which is absent due to pose and garment shape variations. To address this, we introduce five domain-specific metrics: Sharpness (edge clarity via Laplacian variance), Distortion (geometric accuracy using Hough lines and gradient patterns), Texture Preservation (fabric detail via gradient and local binary pattern (LBP) histogram correlation), Pattern Consistency (spatial coherence using FFT spectra correlation), and CLIP Consistency (semantic alignment via CLIP embedding similarity), none of which require ground-truth references.

4.1 QUANTITATIVE EVALUATION

Table 1 presents comprehensive results across all 12 method-dataset combinations, demonstrating consistent improvements in all metrics. Our TTA framework achieves consistent gains: sharpness

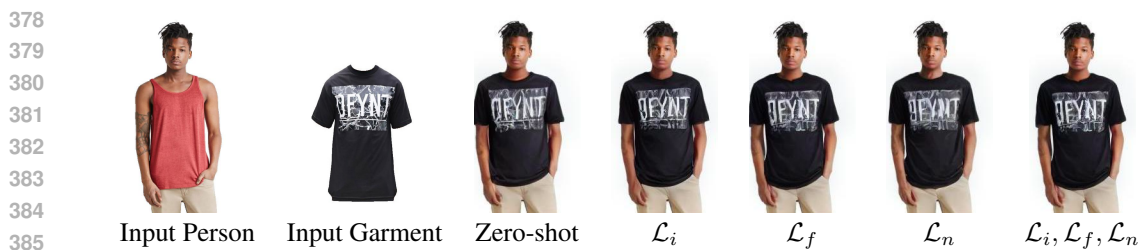


Figure 5: Ablation study visualizing the effect of different loss components on text clarity and pattern preservation. Each loss contributes distinct improvements, with the combination achieving optimal results.

Weight	TPD	LaDI-VTON	Stable-VTON	IDM-VTON
λ_1	20	1000	10	100
λ_2	1000	1000	1000	1000
λ_3	1	0.001	0.001	0.001

Table 2: Hyperparameter values λ_1 , λ_2 , and λ_3 used.

improvements of +7.74% on average, with the largest enhancement being IDM-VTON on VITON-HD (+28.0%), attributed to our DCT loss effectively targeting high-frequency detail preservation. Distortion shows consistent reduction (-0.95%) indicating better geometric accuracy, with the most pronounced improvements on DeepFashion where our neighborhood loss effectively maintains spatial coherence despite challenging in-the-wild conditions. Texture preservation gains (+1.77%) and pattern consistency improvements (+1.09%) demonstrate uniform enhancements across all methods, validating the universal applicability of our statistical loss formulation. CLIP consistency improvements (+1.24%) confirm better semantic alignment between input and generated garments. All metrics are computed only within the garment regions of the input and output garment areas. The universal positive trends across all configurations confirm robust generalization with significantly low failure rates, demonstrating the stability of our optimization process. Additional details are provided in the Appendix for evaluation metrics A, statistical significance C , failure cases G.1, and detailed hyperparameter analysis F are discussed in the Appendix.

4.2 QUALITATIVE ANALYSIS

Figure 4 showcases visual comparisons across all baseline methods, highlighting the effectiveness of our TTA framework in overcoming method-specific limitations. For Stable-VTON, TTA sharpens blurry text and restores accurate colors; for TPD, it enhances pattern integrity and spatial placement, especially in striped or geometric designs. IDM-VTON benefits from improved stripe regularity and reduced distortion, while LaDI-VTON gains more consistent and saturated colors, correcting washed-out or shifted tones. These improvements are most notable under domain shifts in lighting, garment style, texture, and image quality—conditions our method is designed for. TTA consistently preserves fine details like text clarity, pattern sharpness, texture fidelity, and color accuracy, crucial for generated garment quality.

4.3 ABLATION STUDIES

Figure 5 and Table 3 demonstrate the complementary roles of each loss. \mathcal{L}_i enhances global appearance and text clarity through color consistency, \mathcal{L}_f refines textures via high-frequency detail preservation, and \mathcal{L}_n maintains spatial coherence, though it may introduce slight color bleeding in complex areas. Combined, these losses improve text sharpness, color accuracy, and structure. Their contributions vary by garment type: \mathcal{L}_i is more effective for simpler clothing, while \mathcal{L}_f excels with textured garments. Additional details are provided in the Appendix.

4.4 COMPUTATIONAL ANALYSIS

\mathcal{L}_i	\mathcal{L}_f	\mathcal{L}_n	Sharpness	TP	PC	CLIP
\times	\times	\times	0.316	0.753	0.835	0.869
\checkmark	\times	\times	0.361	0.753	0.835	0.880
\times	\checkmark	\times	0.333	0.760	0.856	0.880
\times	\times	\checkmark	0.304	0.761	0.835	0.861
\checkmark	\checkmark	\checkmark	0.368	0.759	0.856	0.889

Table 3: Ablation study results comparing different loss component combinations using TPD on DeepFashion dataset. The complete formulation achieves optimal precision.

Method	VITON-HD		DressCode		DeepFashion		Average
	Paired	Unpaired	Paired	Unpaired	Paired	Unpaired	
TPD	38.8	37.1	30.0	24.4	48.0	42.4	36.8
TPD + TTA	61.2	62.9	70.0	75.6	52.0	57.6	63.2

Table 4: User study results show the percentage of times TTA outputs were preferred over zero-shot generations, highlighting consistent human preference across all datasets.

Figure 6 compares the runtimes of baseline models and their TTA-augmented versions. The added overhead arises from applying guidance at each of the 30 DDIM steps, though this involves only lightweight statistical operations. By using efficient statistical losses—much faster than alternatives like CLIP-based semantic guidance or auxiliary networks—we minimize the computational burden. While our method incurs an overhead compared to zero-shot inference, the amount of overhead is justified by consistent quality gains across diverse domains. The design ensures a practical quality-efficiency trade-off suitable for real-world deployment.

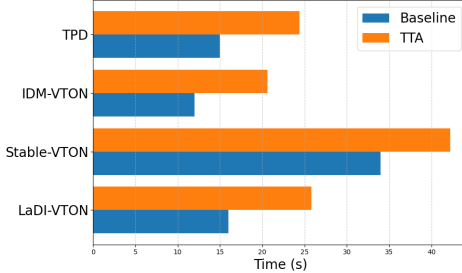


Figure 6: Runtime overhead analysis comparing baseline inference times with that of baseline+TTA.

4.5 LIMITATIONS AND FUTURE WORK

While effective, our TTA framework has limitations. It requires accurate garment masks and lacks suitable validation metrics correlating well with human perception of quality. The current design is limited to single-garment try-on, and extensions to multiple garments may be challenging. Future work will investigate mask-free optimization, multi-garment scenarios, real-time efficiency improvements, and human-validated evaluation metrics. Extension to diverse garment types and integration with foundation models are potential research directions as well.

5 CONCLUSION

We introduced the first test-time adaptation framework for diffusion-based virtual try-on, opening a new research direction where traditional classification-based TTA methods are not applicable. Our computationally efficient approach demonstrates that source parameter-free statistical guidance can improve generation quality without model retraining while maintaining practical deployment feasibility. Our multi-domain loss formulation addresses complementary aspects of garment fidelity, achieving consistent improvements across diverse model architectures and datasets. This work establishes a foundation for adaptive virtual try-on systems that can handle real-world deployment challenges. Future work will explore mask-free adaptation and extension to multi-garment scenarios.

NOTE: LLMs were used to check the manuscript for grammatical errors and restructuring some sentences in the text.

486 REFERENCES
487

- 488 Malik Boudiaf, Romain Mueller, Ismail Ben Ayed, and Luca Bertinetto. Parameter-free online test-
489 time adaptation. In *Proceedings of the IEEE/CVF Conference on Computer Vision and Pattern
490 Recognition (CVPR)*, pp. 8344–8353, June 2022.
- 491 Shoufa Chen, Peize Sun, Yibing Song, and Ping Luo. Diffusiondet: Diffusion model for object
492 detection. In *Proceedings of the IEEE/CVF international conference on computer vision*, pp.
493 19830–19843, 2023a.
- 494 Ziyi Chen, Feng Yu, Minghua Jiang, Hua Wang, Ailing Hua, Tao Peng, Xinrong Hu, and Ping
495 Zhu. Three stages of 3d virtual try-on network with appearance flow and shape field. *The Visual
496 Computer*, 39(8):3545–3559, 2023b.
- 497 Seunghwan Choi, Sunghyun Park, Minsoo Lee, and Jaegul Choo. Viton-hd: High-resolution virtual
498 try-on via misalignment-aware normalization. In *Proceedings of the IEEE/CVF Conference on
499 Computer Vision and Pattern Recognition (CVPR)*, pp. 14131–14140, June 2021.
- 500 Yisol Choi, Sangkyung Kwak, Kyungmin Lee, Hyungwon Choi, and Jinwoo Shin. Improving dif-
501 fusion models for virtual try-on. *arXiv preprint arXiv:2403.05139*, 2024.
- 502 Junhong Gou, Siyu Sun, Jianfu Zhang, Jianlou Si, Chen Qian, and Liqing Zhang. Taming the power
503 of diffusion models for high-quality virtual try-on with appearance flow. In *Proceedings of the
504 31st ACM International Conference on Multimedia*, 2023.
- 505 Xintong Han, Zuxuan Wu, Zhe Wu, Ruichi Yu, and Larry S Davis. Viton: An image-based virtual
506 try-on network. In *Proceedings of the IEEE conference on computer vision and pattern recogni-
507 tion*, pp. 7543–7552, 2018.
- 508 Sen He, Yi-Zhe Song, and Tao Xiang. Style-based global appearance flow for virtual try-on. In
509 *Proceedings of the IEEE/CVF Conference on Computer Vision and Pattern Recognition (CVPR)*,
510 pp. 3470–3479, June 2022.
- 511 Martin Heusel, Hubert Ramsauer, Thomas Unterthiner, Bernhard Nessler, and Sepp Hochreiter.
512 Gans trained by a two time-scale update rule converge to a local nash equilibrium. *Advances in
513 neural information processing systems*, 30, 2017.
- 514 Jonathan Ho, Ajay Jain, and Pieter Abbeel. Denoising diffusion probabilistic models. *Advances in
515 neural information processing systems*, 33:6840–6851, 2020.
- 516 Klara Janouskova, Tamir Shor, Chaim Baskin, and Jiri Matas. Single image test-time adaptation for
517 segmentation. *Transactions on Machine Learning Research*.
- 518 Ansh Khurana, Sujoy Paul, Piyush Rai, Soma Biswas, and Gaurav Aggarwal. Sita: Single image
519 test-time adaptation. *arXiv preprint arXiv:2112.02355*, 2021.
- 520 Jeongho Kim, Guojung Gu, Minho Park, Sunghyun Park, and Jaegul Choo. Stableviton: Learning
521 semantic correspondence with latent diffusion model for virtual try-on. In *Proceedings of the
522 IEEE/CVF Conference on Computer Vision and Pattern Recognition*, pp. 8176–8185, 2024.
- 523 Alexander Kirillov, Eric Mintun, Nikhila Ravi, Hanzi Mao, Chloe Rolland, Laura Gustafson, Tete
524 Xiao, Spencer Whitehead, Alexander C Berg, Wan-Yen Lo, et al. Segment anything. In *Proceed-
525 ings of the IEEE/CVF International Conference on Computer Vision*, pp. 4015–4026, 2023.
- 526 Sangyun Lee, Gyojung Gu, Sunghyun Park, Seunghwan Choi, and Jaegul Choo. High-resolution
527 virtual try-on with misalignment and occlusion-handled conditions. In *European Conference on
528 Computer Vision*, pp. 204–219, 2022.
- 529 Davide Morelli, Matteo Fincato, Marcella Cornia, Federico Landi, Fabio Cesari, and Rita Cucchiara.
530 Dress Code: High-Resolution Multi-Category Virtual Try-On. In *Proceedings of the European
531 Conference on Computer Vision*, 2022.
- 532 Davide Morelli, Alberto Baldrati, Giuseppe Cartella, Marcella Cornia, Marco Bertini, and Rita Cuc-
533 chiara. Ladi-vton: Latent diffusion textual-inversion enhanced virtual try-on. In *Proceedings of
534 the 31st ACM International Conference on Multimedia*, pp. 8580–8589, 2023.

- 540 Muhammad Ferjad Naeem, Seong Joon Oh, Youngjung Uh, Yunjey Choi, and Jaejun Yoo. Reliable
 541 fidelity and diversity metrics for generative models. In *International Conference on Machine*
 542 *Learning*, pp. 7176–7185. PMLR, 2020.
- 543 Assaf Neuberger, Eran Borenstein, Bar Hilleli, Eduard Oks, and Sharon Alpert. Image based virtual
 544 try-on network from unpaired data. In *Proceedings of the IEEE/CVF Conference on Computer*
 545 *Vision and Pattern Recognition (CVPR)*, June 2020.
- 546 Shuaicheng Niu, Jiaxiang Wu, Yifan Zhang, Yaofu Chen, Shijian Zheng, Peilin Zhao, and Mingkui
 547 Tan. Efficient test-time model adaptation without forgetting. In Kamalika Chaudhuri, Stefanie
 548 Jegelka, Le Song, Csaba Szepesvari, Gang Niu, and Sivan Sabato (eds.), *Proceedings of the 39th*
 549 *International Conference on Machine Learning*, volume 162 of *Proceedings of Machine Learning*
 550 *Research*, pp. 16888–16905. PMLR, 17–23 Jul 2022.
- 551 David Osowiechi, Gustavo A. Vargas Hakim, Mehrdad Noori, Milad Cheraghalkhani, Ali Bahri,
 552 Moslem Yazdanpanah, Ismail Ben Ayed, and Christian Desrosiers. Nc-ttt: A noise constrastive
 553 approach for test-time training. In ***, June 2024.
- 554 Robin Rombach, Andreas Blattmann, Dominik Lorenz, Patrick Esser, and Björn Ommer. High-
 555 resolution image synthesis with latent diffusion models. In *Proceedings of the IEEE/CVF confer-*
 556 *ence on computer vision and pattern recognition*, pp. 10684–10695, 2022.
- 557 Sang-Heon Shim, Jiwoo Chung, and Jae-Pil Heo. Towards squeezing-averse virtual try-on via se-
 558 quential deformation. In *Proceedings of the AAAI Conference on Artificial Intelligence*, vol-
 559 ume 38, pp. 4856–4863, 2024.
- 560 Jiaming Song, Chenlin Meng, and Stefano Ermon. Denoising diffusion implicit models. In *Inter-*
 561 *national Conference on Learning Representations*, 2020.
- 562 Junjiao Tian, Lavisha Aggarwal, Andrea Colaco, Zsolt Kira, and Mar Gonzalez-Franco. Diffuse,
 563 attend, and segment: Unsupervised zero-shot segmentation using stable diffusion. *arXiv preprint*
 564 *arXiv:2308.12469*, 2023.
- 565 Yun-Yun Tsai, Fu-Chen Chen, Albert YC Chen, Junfeng Yang, Che-Chun Su, Min Sun, and Cheng-
 566 Hao Kuo. GdA: Generalized diffusion for robust test-time adaptation. In *Proceedings of the*
 567 *IEEE/CVF Conference on Computer Vision and Pattern Recognition*, pp. 23242–23251, 2024.
- 568 Bochao Wang, Huabin Zheng, Xiaodan Liang, Yimin Chen, Liang Lin, and Meng Yang. Toward
 569 characteristic-preserving image-based virtual try-on network. In *Proceedings of the European*
 570 *Conference on Computer Vision (ECCV)*, September 2018.
- 571 Dequan Wang, Evan Shelhamer, Shaoteng Liu, Bruno Olshausen, and Trevor Darrell. Tent: Fully
 572 test-time adaptation by entropy minimization. In *International Conference on Learning Repre-*
 573 *sentations*, 2021. URL <https://openreview.net/forum?id=uXl3bZLkr3c>.
- 574 Zhou Wang, A.C. Bovik, H.R. Sheikh, and E.P. Simoncelli. Image quality assessment: from error
 575 visibility to structural similarity. *IEEE Transactions on Image Processing*, 13(4):600–612, 2004.
 576 doi: 10.1109/TIP.2003.819861.
- 577 Jiazhen Xing, Chao Xu, Yijie Qian, Yang Liu, Guang Dai, Baigui Sun, Yong Liu, and Jingdong
 578 Wang. Tryon-adapter: Efficient fine-grained clothing identity adaptation for high-fidelity virtual
 579 try-on. *arXiv preprint arXiv:2404.00878*, 2024.
- 580 Xu Yang, Changxing Ding, Zhibin Hong, Junhao Huang, Jin Tao, and Xiangmin Xu. Texture-
 581 preserving diffusion models for high-fidelity virtual try-on. In *Proceedings of the IEEE/CVF*
 582 *Conference on Computer Vision and Pattern Recognition*, pp. 7017–7026, 2024.
- 583 Feng Yu, Ailing Hua, Chenghu Du, Minghua Jiang, Xiong Wei, Tao Peng, Lijun Xu, and Xinrong
 584 Hu. Vton-mp: Multi-pose virtual try-on via appearance flow and feature filtering. *IEEE Transac-*
 585 *tions on Consumer Electronics*, 2023.
- 586 Jianhao Zeng, Dan Song, Weizhi Nie, Hongshuo Tian, Tongtong Wang, and An-An Liu. Cat-dm:
 587 Controllable accelerated virtual try-on with diffusion model. In *Proceedings of the IEEE/CVF*
 588 *Conference on Computer Vision and Pattern Recognition*, pp. 8372–8382, 2024.

- 594 Richard Zhang, Phillip Isola, Alexei A Efros, Eli Shechtman, and Oliver Wang. The unreasonable
595 effectiveness of deep features as a perceptual metric. In *CVPR*, 2018.
596
- 597 Fuwei Zhao, Zhenyu Xie, Michael Kampffmeyer, Haoye Dong, Songfang Han, Tianxiang Zheng,
598 Tao Zhang, and Xiaodan Liang. M3d-vton: A monocular-to-3d virtual try-on network. In *Pro-
599 ceedings of the IEEE/CVF International Conference on Computer Vision (ICCV)*, pp. 13239–
600 13249, October 2021.
- 601 Tinghui Zhou, Shubham Tulsiani, Weilun Sun, Jitendra Malik, and Alexei A Efros. View synthesis
602 by appearance flow. In *Computer Vision–ECCV 2016: 14th European Conference, Amsterdam,
603 The Netherlands, October 11–14, 2016, Proceedings, Part IV 14*, pp. 286–301. Springer, 2016.
- 604 Luyang Zhu, Dawei Yang, Tyler Zhu, Fitsum Reda, William Chan, Chitwan Saharia, Mohammad
605 Norouzi, and Ira Kemelmacher-Shlizerman. Tryondiffusion: A tale of two unets. In *Proceedings
606 of the IEEE/CVF Conference on Computer Vision and Pattern Recognition*, pp. 4606–4615, 2023.
- 607
- 608
- 609
- 610
- 611
- 612
- 613
- 614
- 615
- 616
- 617
- 618
- 619
- 620
- 621
- 622
- 623
- 624
- 625
- 626
- 627
- 628
- 629
- 630
- 631
- 632
- 633
- 634
- 635
- 636
- 637
- 638
- 639
- 640
- 641
- 642
- 643
- 644
- 645
- 646
- 647

We present detailed explanations of the metrics used, a convergence analysis for our algorithm, results on the paired setting, additional visual examples along with results of experiments showing the effect of varying certain crucial hyperparameters on the TTA performance, additional generative-based metrics, hyperparameter sensitivity analysis, failure cases, results on other adaptation baselines, and statistical significance evidence for the metrics in the main paper. Codes for implementing our TTA method for IDM-VTON have been included in addition to this document.

A EVALUATION METRICS

Traditional image quality metrics such as SSIM Wang et al. (2004), LPIPS Zhang et al. (2018), and FID Heusel et al. (2017) are inadequate for unpaired virtual try-on evaluation due to the absence of pixel-level correspondence between generated and ground-truth images. The variations in pose, garment shape, and spatial alignment render these metrics ineffective for assessing virtual try-on quality. To address this limitation, we introduce five domain-specific metrics that evaluate different aspects of garment fidelity without requiring spatially aligned ground-truth reference images.

A.1 SHARPNESS

Sharpness quantifies the edge definition in the generated garment regions using the Laplacian variance method. Given a generated image I converted to grayscale G , we compute the Laplacian operator:

$$\nabla^2 G = \frac{\partial^2 G}{\partial x^2} + \frac{\partial^2 G}{\partial y^2} \quad (12)$$

The sharpness metric is defined as the variance of the Laplacian:

$$\text{Sharpness} = \text{Var}(\nabla^2 G) = \frac{1}{N} \sum_{i,j} (\nabla^2 G(i, j) - \mu_{\nabla^2 G})^2 \quad (13)$$

where N is the total number of pixels, $\mu_{\nabla^2 G}$ is the mean of the Laplacian, and higher values indicate sharper images with more defined edges and fine details. The final sharpness values are further divided by 1000 to bring them into a similar scale as other metrics. It is important to note that sharpness values can be unbounded.

A.2 TEXTURE PRESERVATION

Texture preservation evaluates how well the generated garment maintains the texture and surface patterns from the input garment. We employ a multi-component approach combining gradient-based and Local Binary Pattern (LBP) analysis. We compute the gradient magnitude for both generated (G) and input garment (G_{input}) images:

$$|\nabla G| = \sqrt{\left(\frac{\partial G}{\partial x}\right)^2 + \left(\frac{\partial G}{\partial y}\right)^2} \quad (14)$$

The gradient correlation is computed as:

$$\rho_{\text{grad}} = \frac{\text{Cov}(|\nabla G|, |\nabla G_{\text{input}}|)}{\sigma_{|\nabla G|} \sigma_{|\nabla G_{\text{input}}|}} \quad (15)$$

For texture analysis, we compute LBP histograms using uniform patterns with 8 neighbors at radius 1:

$$\text{LBP}_{P,R}(x_c, y_c) = \sum_{p=0}^{P-1} s(g_p - g_c) \cdot 2^p \quad (16)$$

where g_c is the center pixel value, g_p are the neighboring pixel values, and $s(x) = 1$ if $x \geq 0$, else 0. The LBP correlation between normalized histograms is:

$$\rho_{\text{LBP}} = \frac{\sum_i (h_{\text{gen}}[i] - \mu_{\text{gen}})(h_{\text{input}}[i] - \mu_{\text{input}})}{\sqrt{\sum_i (h_{\text{gen}}[i] - \mu_{\text{gen}})^2} \sqrt{\sum_i (h_{\text{input}}[i] - \mu_{\text{input}})^2}} \quad (17)$$

The final texture preservation score combines both components:

$$\text{TP} = 0.6 \cdot \max(0, \rho_{\text{grad}}) + 0.4 \cdot \max(0, \rho_{\text{LBP}}) \quad (18)$$

702 A.3 DISTORTION
 703

704 Distortion measures geometric artifacts and spatial inconsistencies in the generated garment using
 705 edge analysis and gradient consistency. The metric combines edge-based and gradient-based distortion
 706 detection. We detect edges using the Canny edge detector and analyze line patterns using the
 707 Hough transform. For detected lines with endpoints (x_1, y_1) and (x_2, y_2) , we compute angles:

$$\theta = \arctan\left(\frac{y_2 - y_1}{x_2 - x_1}\right) \cdot \frac{180}{\pi} \quad (19)$$

711 The edge distortion is quantified by the variance of line angles:

$$D_{\text{edge}} = \min\left(1.0, \frac{\text{Var}(\theta)}{1000}\right) \quad (20)$$

715 **Gradient-based Distortion** We analyze gradient consistency using the coefficient of variation:

$$CV_{\text{grad}} = \frac{\sigma_{|\nabla G|}}{\mu_{|\nabla G|}} \quad (21)$$

719 where $\sigma_{|\nabla G|}$ and $\mu_{|\nabla G|}$ are the standard deviation and mean of the gradient magnitude, respectively.
 720 The final distortion score (inverted for quality assessment) is:

$$\text{Distortion} = 1.0 - \min(1.0, \max(0.0, 0.7 \cdot D_{\text{edge}} + 0.3 \cdot \min(1.0, CV_{\text{grad}}/2.0))) \quad (22)$$

723 A.4 PATTERN CONSISTENCY
 724

725 Pattern consistency evaluates the preservation of spatial frequency patterns and periodic struc-
 726 tures using Fast Fourier Transform (FFT) analysis. Given input and generated garment images in
 727 grayscale, we compute their 2D FFTs:

$$F_{\text{input}}(u, v) = \sum_{x=0}^{M-1} \sum_{y=0}^{N-1} G_{\text{input}}(x, y) e^{-j2\pi(ux/M+vy/N)} \quad (23)$$

$$F_{\text{gen}}(u, v) = \sum_{x=0}^{M-1} \sum_{y=0}^{N-1} G_{\text{gen}}(x, y) e^{-j2\pi(ux/M+vy/N)} \quad (24)$$

735 The magnitude spectra are computed as:

$$|F_{\text{input}}(u, v)| = \sqrt{\text{Re}(F_{\text{input}}(u, v))^2 + \text{Im}(F_{\text{input}}(u, v))^2} \quad (25)$$

738 Pattern consistency is measured by the correlation between flattened magnitude spectra:

$$\text{PC} = \max(0, \rho(|F_{\text{input}}|, |F_{\text{gen}}|)) \quad (26)$$

741 where ρ denotes the Pearson correlation coefficient.

743 A.5 CLIP CONSISTENCY
 744

745 CLIP consistency measures semantic alignment between the input garment and generated garment
 746 using pre-trained CLIP vision encoders. Given input garment image I_{garment} and generated image
 747 I_{gen} , we extract feature representations:

$$f_{\text{garment}} = \text{CLIP}_{\text{vision}}(I_{\text{garment}}) \quad (27)$$

$$f_{\text{gen}} = \text{CLIP}_{\text{vision}}(I_{\text{gen}}) \quad (28)$$

751 The CLIP consistency is computed as the cosine similarity between L2-normalized feature vectors:

$$\text{CLIP Consistency} = \max(0, \frac{f_{\text{garment}} \cdot f_{\text{gen}}}{\|f_{\text{garment}}\|_2 \|f_{\text{gen}}\|_2}) \quad (29)$$

752 This metric captures high-level semantic similarity while being robust to spatial misalignments,
 753 making it particularly suitable for evaluating unpaired virtual try-on generation quality.

756 A.6 METRIC COMPUTATION DETAILS
 757

758 All metrics are computed exclusively within garment regions using binary masks to focus evaluation
 759 on relevant areas. For texture preservation and pattern consistency, input and generated garments
 760 are resized to match dimensions when necessary. The metrics are designed to be robust to illumina-
 761 tion changes and minor spatial variations while being sensitive to quality degradation in texture,
 762 sharpness, geometric consistency, and semantic alignment. Together, these five metrics provide a
 763 comprehensive assessment of virtual try-on quality without requiring pixel-level ground-truth cor-
 764 respondence.

765 B CONVERGENCE ANALYSIS
 766

768 We provide theoretical foundations for the convergence of our TTA guidance process, including
 769 derivations of smoothness constants for each loss component.

770 B.1 THEORETICAL FRAMEWORK
 771

772 Our guidance update follows:

$$773 \quad \mathbf{x}_{t-1}^g = \hat{\mathbf{x}}_{t-1}^g - \alpha \nabla_{\mathbf{x}_{0,t}^g} \mathcal{L}(\mathbf{x}_{0,t}^g, \mathbf{x}_0) \quad (30)$$

775 where $\mathcal{L}(\mathbf{x}_{0,t}^g, \mathbf{x}_0) = \lambda_1 \mathcal{L}_i + \lambda_2 \mathcal{L}_f + \lambda_3 \mathcal{L}_n$, where each of the losses corresponds to the image space
 776 histogram loss, frequency domain loss, and the neighborhood loss, respectively.

777 **Theorem B.1** (Convergence Guarantee). *Assume the combined loss function $\mathcal{L}(\mathbf{x}_{0,t}^g, \mathbf{x}_0)$ is L -
 778 smooth. Then for learning rate $\alpha \leq \frac{1}{L}$, the guidance process satisfies:*

$$779 \quad \mathcal{L}(\mathbf{x}_{t+1}^g, \mathbf{x}_0) \leq \mathcal{L}(\mathbf{x}_t^g, \mathbf{x}_0) - \frac{\alpha}{2} \|\nabla \mathcal{L}(\mathbf{x}_t^g, \mathbf{x}_0)\|^2$$

780 and converges to a stationary point with rate:

$$781 \quad \min_{0 \leq k \leq T} \|\nabla \mathcal{L}(\mathbf{x}_{0,k}^g, \mathbf{x}_0)\|^2 \leq \frac{2L(\mathcal{L}(\mathbf{x}_{0,0}^g, \mathbf{x}_0) - \mathcal{L}^*)}{T} \quad (31)$$

785 *Proof.* Let $\mathbf{g}_t = \nabla \mathcal{L}(\mathbf{x}_t^g, \mathbf{x}_0)$. From L -smoothness of \mathcal{L} we have:

$$786 \quad \mathcal{L}(\mathbf{x}_{t+1}^g, \mathbf{x}_0) \leq \mathcal{L}(\mathbf{x}_t^g, \mathbf{x}_0) + \nabla \mathcal{L}(\mathbf{x}_t^g, \mathbf{x}_0)^T (\mathbf{x}_{t+1}^g - \mathbf{x}_t^g) \quad (32)$$

$$787 \quad - \mathbf{x}_t^g) + \frac{L}{2} \|\mathbf{x}_{t+1}^g - \mathbf{x}_t^g\|^2 \quad (33)$$

788 Substituting the update rule $\mathbf{x}_{t+1}^g - \mathbf{x}_t^g = -\alpha \mathbf{g}_t$ gives us:

$$789 \quad \begin{aligned} \mathcal{L}(\mathbf{x}_{t+1}^g, \mathbf{x}_0) &\leq \mathcal{L}(\mathbf{x}_t^g, \mathbf{x}_0) + \mathbf{g}_t^T (-\alpha \mathbf{g}_t) + \frac{L}{2} \|-\alpha \mathbf{g}_t\|^2 \\ &= \mathcal{L}(\mathbf{x}_t^g, \mathbf{x}_0) - \alpha \|\mathbf{g}_t\|^2 + \frac{L\alpha^2}{2} \|\mathbf{g}_t\|^2 \\ &= \mathcal{L}(\mathbf{x}_t^g, \mathbf{x}_0) - \alpha \left(1 - \frac{L\alpha}{2}\right) \|\mathbf{g}_t\|^2 \end{aligned} \quad (34)$$

790 For $\alpha \leq \frac{2}{L}$, we have $1 - \frac{L\alpha}{2} \geq 0$. For $\alpha \leq \frac{1}{L}$, we have $1 - \frac{L\alpha}{2} \geq \frac{1}{2}$, giving:

$$791 \quad \mathcal{L}(\mathbf{x}_{t+1}^g, \mathbf{x}_0) \leq \mathcal{L}(\mathbf{x}_t^g, \mathbf{x}_0) - \frac{\alpha}{2} \|\mathbf{g}_t\|^2 \quad (35)$$

792 We have:

$$793 \quad \sum_{t=0}^{T-1} \|\mathbf{g}_t\|^2 \leq \frac{2(\mathcal{L}(\mathbf{x}_0^g, \mathbf{x}_0) - \mathcal{L}^*)}{\alpha} \quad (36)$$

794 Using the telescopic cancellation trick over T steps and taking the minimum of the squared norm of
 795 the gradient of the loss gives us the result. \square

796 We also provide derivations for the smoothness constants of each loss component, which are
 797 essential for proving the convergence guarantees.

810 **B.2 IMAGE-SPACE LOSS SMOOTHNESS (\mathcal{L}_i)**
 811

812 The image-space loss is defined as:

813
 814
$$\mathcal{L}_i = \frac{1}{3} \sum_{c=1}^3 \frac{1}{N_b} \sum_{j=1}^{N_b} |h_j^c(\mathcal{X}, N_b) - h_j^c(\mathcal{Y}, N_b)| \quad (37)$$

 815

816 The histogram function $h_j^c(\mathcal{Y}, N_b)$ involves discrete binning operations, making it non-
 817 differentiable. In order to address this, we employ a smoothed histogram approximation using a
 818 kernel function.

819 **Lemma B.2.** *A smoothed histogram can be obtained by replacing the hard binning (non-
 820 differentiable) with a soft binning by applying a Gaussian kernel:*

822
 823
$$h_k^c(\mathcal{Y}, N_b) \approx \frac{1}{|\mathcal{Y}|} \sum_{(i,j) \in \mathcal{Y}} K_\sigma \left(\frac{y_{i,j}^c \cdot N_b}{M} - k \right) \quad (38)$$

 824

825 where $K_\sigma(u) = \frac{1}{\sqrt{2\pi\sigma^2}} e^{-u^2/(2\sigma^2)}$ is a Gaussian kernel with standard deviation σ , and M is the
 826 range of pixel intensities.

827 *Proof.* We first compute the derivative of the smoothed histogram:

829
 830
$$\frac{\partial h_k^c}{\partial y_{i,j}^c} = \frac{1}{|\mathcal{Y}|} \cdot \frac{N_b}{M} \cdot K'_\sigma \left(\frac{y_{i,j}^c \cdot N_b}{M} - k \right) \quad (39)$$

 831

832 The next step is to bound the kernel derivative. For the Gaussian kernel that we use, we have

833
 834
$$K'_\sigma(u) = -\frac{u}{\sigma^2} K_\sigma(u) \quad (40)$$

835 The maximum absolute value occurs at $|u| = \sigma$:

836
 837
$$\max_u |K'_\sigma(u)| = \frac{1}{\sigma\sqrt{2\pi e\sigma^2}} \leq \frac{C_1}{\sigma^2} \quad (41)$$

 838

839 where the constant $C_1 = 1/\sqrt{2\pi e}$ is the maximum possible value of the kernel. The L1 norm gives
 840 us a Lipschitz constant of 1, because:

841
 842
$$\left| \frac{d}{dx} |x| \right| = |\text{sign}(x)| = 1 \quad (42)$$

 843

844 Combining all the expressions mentioned above, we have:

845
 846
$$\frac{\partial h_k^c}{\partial y_{i,j}^c} = \frac{1}{|\mathcal{Y}|} \cdot \frac{N_b}{M} \cdot K'_\sigma \left(\frac{y_{i,j}^c \cdot N_b}{M} - k \right) \quad (43)$$

 847

848 And we established:

849
$$\max_u |K'_\sigma(u)| = \frac{C_1}{\sigma^2} \text{ where } C_1 = \frac{1}{\sqrt{2\pi e}} \quad (44)$$

850 Now, for the total smoothness constant:

851
 852
$$L_i = \frac{\partial \mathcal{L}_i}{\partial y_{i,j}^c}$$

 853
 854
$$= \frac{\partial}{\partial y_{i,j}^c} \left[\frac{1}{3} \sum_{c=1}^3 \frac{1}{N_b} \sum_{j=1}^{N_b} |h_j^c(\mathcal{X}, N_b) - h_j^c(\mathcal{Y}, N_b)| \right] \quad (45)$$

 855
 856

857 Since the L1 norm has derivative bounded by 1 in magnitude:

859
 860
$$L_i \leq \frac{1}{3} \sum_{c=1}^3 \frac{1}{N_b} \sum_{j=1}^{N_b} \left| \frac{\partial h_j^c(\mathcal{Y}, N_b)}{\partial y_{i,j}^c} \right| \quad (46)$$

 861

862
 863
$$= \frac{1}{3} \sum_{c=1}^3 \frac{1}{N_b} \sum_{j=1}^{N_b} \left| \frac{1}{|\mathcal{Y}|} \cdot \frac{N_b}{M} \cdot K'_\sigma \left(\frac{y_{i,j}^c \cdot N_b}{M} - j \right) \right| \quad (47)$$

864 For a single pixel (i, j) and channel c , when we consider all the N_b histogram bins, we get:
 865

$$866 \quad L_i \leq \frac{1}{3} \sum_{c=1}^3 \frac{1}{N_b} \sum_{j=1}^{N_b} \frac{1}{|\mathcal{Y}|} \cdot \frac{N_b}{M} \cdot \frac{C_1}{\sigma^2} \quad (48)$$

$$869 \quad = \frac{1}{|\mathcal{Y}|} \frac{N_b C_1}{M \sigma^2} \quad (49)$$

871 Since the cardinality $|\mathcal{Y}| \approx |\Omega|$ (the masked garment region size):
 872

$$873 \quad L_i \leq \frac{C N_b}{|\Omega|} \quad (50)$$

876 where $C = \frac{C_1}{M \cdot \sigma^2}$. □
 877

879 B.3 FREQUENCY-DOMAIN LOSS SMOOTHNESS (\mathcal{L}_f) 880

881 The frequency-domain loss is:
 882

$$883 \quad \mathcal{L}_f = \frac{1}{N_b} \sum_{j=1}^{N_b} |h_j(\mathcal{S}_i, N_b) - h_j(\mathcal{S}_g, N_b)| \quad (51)$$

886 where $\mathcal{S}_g = \{\text{DCT-1D}(\text{DCT-2D}(\hat{\mathbf{y}}_b, K))\}$.
 887

888 **Lemma B.3** (DCT Jacobian Bounds). *For a $K \times K$ block \mathbf{B} , the 2D DCT operation has bounded
 889 derivatives:*

$$890 \quad \left| \frac{\partial \text{DCT-2D}(\mathbf{B})_{u,v}}{\partial \mathbf{B}_{i,j}} \right| = \left| \cos \left(\frac{\pi u(2i+1)}{2K} \right) \cos \left(\frac{\pi v(2j+1)}{2K} \right) \right| \\ 891 \quad \leq 1 \quad (52)$$

894 The DCT is applied as follows:
 895

- 896 1. 2D DCT on $K \times K$ spatial blocks: All Jacobian entries bounded by 1
 897
- 898 2. 1D DCT along channel dimension: All Jacobian entries bounded by 1
 899
- 900 3. Flattening operation (just to get a set of coefficients for computing the histogram): the
 901 Jacobian is still bounded above by 1

902 *Proof.* The frequency loss is:
 903

$$904 \quad \mathcal{L}_f = \frac{1}{N_b} \sum_{j=1}^{N_b} |h_j(\mathcal{S}_i, N_b) - h_j(\mathcal{S}_g, N_b)| \quad (53)$$

907 where N_b is the number of frequency domain histogram bins. A pixel (i, j) in channel c affects one
 908 $K \times K$ block. Within that block, at position (i', j') :

$$910 \quad \frac{\partial \text{DCT}_{u,v}}{\partial y_{i,j}^c} = \cos \left(\frac{\pi u(2i'+1)}{2K} \right) \cos \left(\frac{\pi v(2j'+1)}{2K} \right) \quad (54)$$

913 Each coefficient derivative is bounded by 1, and there are K^2 coefficients per block. After 1D-
 914 DCT along channels and flattening, one pixel affects K^2 DCT coefficients (all which have bounded
 915 derivatives). Each DCT coefficient s_k contributes to the histogram:

$$917 \quad \left| \frac{\partial h_j}{\partial s_k} \right| \leq \frac{1}{|\mathcal{S}_g|} \cdot \frac{N_b}{s_{\max} - s_{\min}} \cdot \frac{C_2}{\sigma^2} \quad (55)$$

The above equation follows from the previous part's derivation for \mathcal{L}_i . One pixel affects K^2 DCT coefficients, each affecting all N_b histogram bins:

$$\left| \frac{\partial \mathcal{L}_f}{\partial y_{i,j}^c} \right| \leq \frac{1}{N_b} \sum_{j=1}^{N_b} \sum_{k=1}^{K^2} \left| \frac{\partial h_j}{\partial s_k} \right| \cdot \left| \frac{\partial s_k}{\partial y_{i,j}^c} \right| \quad (56)$$

$$\leq \frac{1}{N_b} \cdot N_b \cdot K^2 \cdot \frac{1}{|\mathcal{S}_g|} \cdot \frac{N_b}{s_{\max} - s_{\min}} \cdot \frac{C_2}{\sigma^2} \cdot 1 \quad (57)$$

$$= K^2 \cdot \frac{N_b}{|\mathcal{S}_g|} \cdot \frac{C_2}{\sigma^2} \quad (58)$$

Since $|\mathcal{S}_g| \approx \frac{|\Omega|}{K^2} \cdot K^2 = |\Omega|$ (total DCT coefficients):

$$L_f \leq \frac{K^2 \cdot N_b \cdot C_2}{|\Omega| \cdot \sigma^2} \quad (59)$$

Setting $C_f = \frac{C_2}{\sigma^2}$ we get:

$$L_f \leq \frac{C_f K^2 N_b}{|\Omega|} \quad (60)$$

□

B.4 NEIGHBORHOOD LOSS SMOOTHNESS (\mathcal{L}_n)

The neighborhood loss is the KL-divergence between Gaussian distributions:

$$\mathcal{L}_n = \frac{1}{2} \left(\text{tr}(\Sigma_g^{-1} \Sigma_i) + (\mu_g - \mu_i)^T \Sigma_g^{-1} (\mu_g - \mu_i) \right) \quad (61)$$

$$- d + \ln \frac{\det \Sigma_g}{\det \Sigma_i} \quad (62)$$

Proof. For the sample mean $\mu_g = \frac{1}{N} \sum_{k=1}^N \mathbf{v}_k^g$ where \mathbf{v}_k^g are d -dimensional neighborhood vectors, each pixel affects at most d neighborhoods, giving $\left\| \frac{\partial \mu_g}{\partial y_{i,j}^c} \right\| \leq \frac{d}{N}$. For the covariance matrix $\Sigma_g = \frac{1}{N-1} \sum_{k=1}^N (\mathbf{v}_k^g - \mu_g)(\mathbf{v}_k^g - \mu_g)^T$, we have

$$\left\| \frac{\partial \Sigma_g}{\partial y_{i,j}^c} \right\|_F \leq \frac{C_3 \cdot d}{N} \quad (63)$$

where C_3 depends on the variance of neighborhood vectors, and $\|\cdot\|_F$ is the Frobenius norm. For the trace term, using the matrix calculus identity $\frac{\partial \text{tr}(\mathbf{A}^{-1} \mathbf{B})}{\partial \mathbf{A}} = -\mathbf{A}^{-1} \mathbf{B} \mathbf{A}^{-1}$ for symmetric matrices:

$$\frac{\partial \text{tr}(\Sigma_g^{-1} \Sigma_i)}{\partial y_{i,j}^c} = -(\Sigma_g^{-1} \Sigma_i \Sigma_g^{-1}) \frac{\partial \Sigma_g}{\partial y_{i,j}^c} \quad (64)$$

which gives:

$$\left| \frac{\partial \text{tr}(\Sigma_g^{-1} \Sigma_i)}{\partial y_{i,j}^c} \right| \leq \frac{\|\Sigma_i\|_2 C_3 d}{\sigma_{\min}(\Sigma_g)^2 N} \quad (65)$$

For the quadratic term with $\Delta = \mu_g - \mu_i$:

$$\frac{\partial (\Delta^T \Sigma_g^{-1} \Delta)}{\partial y_{i,j}^c} = 2\Delta^T \Sigma_g^{-1} \frac{\partial \mu_g}{\partial y_{i,j}^c} - \Delta^T \Sigma_g^{-1} \frac{\partial \Sigma_g}{\partial y_{i,j}^c} \Sigma_g^{-1} \Delta \quad (66)$$

which is bounded by $\frac{2\|\Delta\|d}{\sigma_{\min}(\Sigma_g)N} + \frac{\|\Delta\|^2 C_3 d}{\sigma_{\min}(\Sigma_g)^2 N}$. For the determinant term:

$$\frac{\partial \ln \det \Sigma_g}{\partial y_{i,j}^c} = \text{tr} \left(\Sigma_g^{-1} \frac{\partial \Sigma_g}{\partial y_{i,j}^c} \right) \quad (67)$$

972
973
Table 5: Evidence of Test-Time Adaptation Improvements for Image Quality Metrics
974

Method	Metric	Improvement	Rel. (%)	Effect Size	Consistency	P(+)	Evidence
IDM-VTON	Sharpness	+0.1014	+26.61	0.508 (medium)	3/3	0.81	Strong
	Distortion	-0.0057	-10.54	-0.482 (small)	3/3	0.90	Strong
LaDI-VTON	Sharpness	+0.0707	+16.27	0.700 (medium)	3/3	0.83	Strong
	Distortion	-0.0053	-10.20	-0.739 (medium)	2/3	0.80	Strong
Stable-VITON	Sharpness	+0.0041	+1.00	0.056 (negligible)	3/3	0.90	Moderate
	Distortion	-0.0024	-5.83	-0.777 (medium)	3/3	0.83	Strong
TPD	Sharpness	+0.0244	+6.65	0.342 (small)	3/3	0.89	Strong
	Distortion	-0.0055	-10.75	-0.644 (medium)	3/3	0.95	Strong

983
984
985 which is bounded by $\frac{C_3 d}{\sigma_{\min}(\Sigma_g) N}$.986
987 Combining all terms, the dominant scaling comes from the $\sigma_{\min}(\Sigma_g)^{-2}$ terms, giving:

988
989
$$L_n \leq \frac{C_n}{\sigma_{\min}(\Sigma_g)^2} \quad (68)$$

990
991 where C_n depends on the neighborhood dimension d , sample size N , and the norms of Σ_i and
992 $\mu_g - \mu_i$. Combining all terms and noting that $\ln \det \Sigma_i$ doesn't depend on $y_{i,j}^c$:

993
994
$$\left| \frac{\partial \mathcal{L}_n}{\partial y_{i,j}^c} \right| \leq \frac{1}{2} \left[\frac{\|\Sigma_i\|_2 C_3 d}{\sigma_{\min}(\Sigma_g)^2 N} + \frac{2\|\Delta\|d}{\sigma_{\min}(\Sigma_g)N} \right] \quad (69)$$

995
996
$$+ \frac{\|\Delta\|^2 C_3 d}{\sigma_{\min}(\Sigma_g)^2 N} + \frac{C_3 d}{\sigma_{\min}(\Sigma_g)N} \quad (70)$$

997
998 The dominant terms scale as $\frac{1}{\sigma_{\min}(\Sigma_g)^2}$, giving:
1000

1001
1002
$$L_n \leq \frac{C_n}{\sigma_{\min}(\Sigma_g)^2} \quad (71)$$

1003
1004 where C_n depends on d, N , and the norms of Σ_i and $\mu_g - \mu_i$. \square 1005
1006 **Corollary B.3.1** (Combined Smoothness Constant). *The combined loss $\mathcal{L} = \lambda_1 \mathcal{L}_i + \lambda_2 \mathcal{L}_f + \lambda_3 \mathcal{L}_n$ is L -smooth with:*

1007
1008
$$L = \lambda_1 L_i + \lambda_2 L_f + \lambda_3 L_n \leq \lambda_1 \frac{CN_b}{|\Omega|} + \lambda_2 \frac{C_f K^2 N_b}{|\Omega|} + \lambda_3 \frac{C_n}{\sigma_{\min}(\Sigma_g)^2} \quad (72)$$

1012
B.5 EMPIRICAL VALIDATION1013
1014 Despite the conservative theoretical bounds, our method demonstrates stable convergence across all
1015 the diffusion-based try-on models (IDM-VTON, LaDI-VTON, Stable-VITON, TPD) and datasets
1016 (VITON-HD, DressCode, DeepFashion) with learning rates much larger than theoretical predictions.
1017 This consistent empirical success suggests the actual optimization benefits from favorable
1018 attributes not captured by worst-case smoothness bounds. Our convergence analysis provides a
1019 theoretical foundation and conservative guarantees for the TTA guidance process. While these bounds
1020 are conservative compared to empirical practice, they offer valuable insights into the optimization
1021 dynamics and serve as a starting point for hyperparameter selection.1022
C STATISTICAL EVIDENCE FOR TEST-TIME ADAPTATION BENEFITS1023
1024
1025 Despite the limited sample size (n=3 datasets), multiple converging lines of evidence demonstrate
meaningful improvements from test-time adaptation (TTA) across important image quality metrics.

Our analysis utilizes effect size estimation, cross-dataset consistency assessment, and Bayesian evidence evaluation to provide robust statistical inference beyond traditional significance testing. In Table 5, consistency represents the number of datasets showing improvement out of 3 total, $P(+)$ denotes the Bayesian posterior probability of positive effect, and for distortion metrics, lower values indicate better quality. Evidence strength is classified as Strong when effect sizes exceed 0.3 with high consistency, and Moderate when we observe mixed evidence patterns.

C.1 SHARPNESS ENHANCEMENT

TTA demonstrates substantial sharpness improvements across all methods, with the most dramatic gains observed in IDM-VTON (+26.61%) and LaDI-VTON (+16.27%). These methods achieve medium effect sizes (Cohen’s $d = 0.51$ and 0.70 respectively), indicating practically significant improvements. Crucially, sharpness enhancement shows perfect consistency across all datasets (3/3) for every method, with high Bayesian posterior probabilities ($P(\text{improvement}) = 0.81\text{--}0.90$), providing compelling evidence for reliable image quality enhancement.

C.2 DISTORTION REDUCTION

All methods demonstrate consistent distortion reduction, with relative improvements ranging from 5.83% to 10.75%. The effect sizes are consistently medium-to-large ($d = 0.48\text{--}0.78$), indicating substantial practical impact. While traditional consistency metrics show mixed results due to the directional nature of this metric (lower distortion = better quality), the Bayesian analysis reveals strong evidence for improvement ($P(\text{improvement}) = 0.80\text{--}0.95$ for most methods), suggesting robust distortion mitigation across different virtual try-on approaches.

C.3 CONVERGENT EVIDENCE PATTERN

The combination of substantial effect sizes, high directional consistency, and strong Bayesian evidence provides a compelling case for TTA effectiveness. Notably, IDM-VTON and LaDI-VTON show the strongest evidence patterns, with medium effect sizes for both metrics and perfect dataset consistency for sharpness improvements. Even Stable-VITON, despite modest sharpness gains, demonstrates strong distortion reduction with a large effect size ($d = -0.78$). This evidence suggests that test-time adaptation offers reliable and meaningful improvements in visual quality, with particularly strong support for enhanced image sharpness and reduced geometric distortion across diverse virtual try-on baseline methods.

D PAIRED SETTING EVALUATION

Method	VITON-HD		DressCode		DeepFashion	
	LPIPS	SSIM	LPIPS	SSIM	LPIPS	SSIM
LaDI-VTON	0.1566	0.8785	0.1676	0.8862	0.1088	0.8913
LaDI-VTON + TTA	0.1562	0.8775	0.1498	0.8955	0.0899	0.9083
TPD	0.1473	0.8859	0.0855	0.9613	0.0684	0.9268
TPD + TTA	0.1481	0.8875	0.0893	0.9537	0.0681	0.9282
IDM-VTON	0.1464	0.8902	0.1166	0.9211	0.1260	0.9121
IDM-VTON + TTA	0.1326	0.8896	0.1099	0.9323	0.1020	0.9279
Stable VITON	0.2065	0.8949	0.2329	0.8903	0.1819	0.9070
Stable VITON + TTA	0.2069	0.8956	0.2312	0.8896	0.1791	0.9068

Table 6: Performance comparison in the paired setting, where reference-based metrics are used for evaluation.

We also evaluate our method in the paired setting using ground-truth references. SSIM Wang et al. (2004) and LPIPS Zhang et al. (2018) scores on all three datasets are reported in Table 6. Even with reference-based metrics, our TTA approach yields improvements in most cases alongside visual quality, further validating its effectiveness.

1080 **E HYPERPARAMETER SENSITIVITY**
 1081

1082 We analyze the sensitivity of loss weight hyperparameters in Table 8, using a deviation threshold of
 1083 less than 10^{-3} in sharpness, texture preservation, and pattern consistency metrics. The results show
 1084 that performance remains stable across a broad range of values for λ_1 , λ_2 , and λ_3 , indicating that
 1085 TTA guidance is robust to variations in loss weighting.

1087 **F EFFECT OF HYPERPARAMETERS**
 1088

1089 Since each baseline method requires different scales of baseline loss values, the hyperparameters
 1090 need to be tuned appropriately for the TTA guidance. The weights used for each baseline method
 1091 are listed in Table 7. The hyperparameters are kept constant across all datasets for a given method.
 1092

Weight	TPD	LaDI-VTON	Stable-VTON	IDM-VTON
λ_1	25	1000	10	100
λ_2	1000	1000	1000	1000
λ_3	1	0.001	0.001	0.001

1093 Table 7: Hyperparameter values λ_1 , λ_2 , and λ_3 for each method.
 1094
 1095

Weight	TPD	LaDI-VTON	Stable-VTON	IDM-VTON
λ_1	5-50	750-1250	10	100
λ_2	750-2000	750-2000	750-2250	750-1250
λ_3	0.5-2	$5 \times 10^{-4} - 2 \times 10^{-3}$	$5 \times 10^{-4} - 2 \times 10^{-3}$	$5 \times 10^{-4} - 2 \times 10^{-3}$

1096 Table 8: Hyperparameter values λ_1 , λ_2 , and λ_3 for each method.
 1097
 1098

1100 **F.1 EFFECT OF NEIGHBORHOOD SIZE**
 1101

1102 For all experiments, we consider neighborhoods of dimension $\sqrt{d} \times \sqrt{d}$, which are flattened into
 1103 d -dimensional vectors. Using vectors obtained from non-overlapping neighborhoods in the garment
 1104 regions of both the input and generated images, we estimate two Gaussian distributions and attempt
 1105 to match them through the diffusion guidance. Table 9 shows that a neighborhood size of 2×2
 1106

\sqrt{d}	Sharpness	TP	PC	CLIP
2	0.368	0.759	0.856	0.889
3	0.368	0.753	0.856	0.886
4	0.369	0.753	0.856	0.889
5	0.369	0.753	0.853	0.888

1107 Table 9: Performance comparison of TTA with different neighborhood block-sizes in the loss \mathcal{L}_n .
 1108 Best values are bolded.
 1109

1110 $(\sqrt{d} = 2)$ achieves the best texture preservation and CLIP consistency scores while maintaining
 1111 competitive sharpness and pattern consistency. While larger neighborhood sizes ($\sqrt{d} = 4, 5$)
 1112 achieve marginally higher sharpness scores, they suffer from reduced texture preservation quality.
 1113 A small neighborhood size ensures that fine-grained local structure and texture details are retained
 1114 in the generated images, whereas a large neighborhood size can lead to a loss of texture fidelity and
 1115 reduced semantic consistency, as shown in Figure 7.
 1116

1117 **Effect of DCT Block Size:** The frequency-domain loss \mathcal{L}_f helps in preserving high-frequency
 1118 details like edges and patterns in the generated images. While it is beneficial to have a large block
 1119 size K ($K \times K$ dimensional) to capture all frequency components in the image effectively, it
 1120 comes at the cost of computation time. We observe that the generations for $K = 32, 48, 64$ appear
 1121 roughly the same in terms of CLIP consistency while $K = 16$ results in poorer sharpness and CLIP
 1122 alignment. From Table 10, we observe that a block size of $K = 32$ offers the best balance across all
 1123

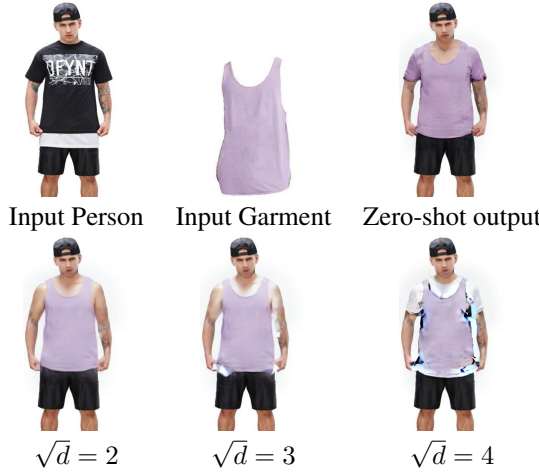


Figure 7: Visual results of using different neighborhood sizes. If the neighborhood is too large, color bleeding can occur.

K	Sharpness	TP	PC	CLIP
16	0.342	0.757	0.858	0.883
32	0.368	0.759	0.856	0.889
48	0.361	0.751	0.856	0.889
64	0.359	0.739	0.856	0.889

Table 10: Performance comparison of TTA with different DCT block-sizes in the loss \mathcal{L}_f . Best values are bolded.

metrics, achieving the highest sharpness and texture preservation scores while maintaining strong CLIP consistency. This suggests that $K = 32$ captures frequency components effectively without compromising texture quality or computational efficiency.

Effect of Guidance Time-Steps: We analyze the number of diffusion guidance time-steps for optimizing our TTA objective. From Table 11, we observe that $T = 30$ time-steps provide an

T	Sharpness	TP	PC	CLIP
10	0.319	0.702	0.817	0.889
20	0.343	0.740	0.822	0.883
30	0.368	0.759	0.856	0.889
40	0.368	0.761	0.854	0.883
50	0.367	0.761	0.856	0.888

Table 11: Performance comparison of TTA with different diffusion guidance time-steps T . Best values are bolded.

optimal balance across all quality metrics, achieving the best sharpness and pattern consistency while maintaining competitive texture preservation and CLIP consistency scores. While $T = 40, 50$ show marginally better texture preservation, they suffer from reduced CLIP alignment and pattern consistency. This aligns with the overall loss function curves, which were observed to converge at $T = 30$ time steps for nearly all examples. Increasing the number of time steps beyond 30 led to overtraining during test-time, causing artifacts to appear along the boundaries of garment regions and reduced semantic consistency.

Effect of Number of Bins: The number of histogram bins for both the image and frequency-domain losses affects the performance of TTA at a distributional level. Tables 12 and 13 show the effect of changing the number of bins on the TTA performance. In the case of the image histogram, it is op-

1188
 1189 optimal to have $N_b = 100$ bins since this configuration achieves strong performance across sharpness,
 1190 texture preservation, and pattern consistency metrics while maintaining competitive CLIP scores.
 1191 A moderate bin count provides sufficient granularity for color distribution matching without intro-

N_b	Sharpness	TP	PC	CLIP
50	0.362	0.759	0.855	0.890
100	0.368	0.759	0.856	0.889
150	0.368	0.759	0.849	0.888
200	0.371	0.751	0.839	0.888
250	0.368	0.720	0.831	0.890

1198
 1199 Table 12: Performance comparison of TTA with different bins N_b in the image-space histogram loss
 1200 \mathcal{L}_i . Best values are bolded.

1201 ducing noise or artifacts. While higher bin counts ($N_b = 200$) achieve marginally better sharpness,
 1202 they compromise texture preservation and pattern consistency. On the other hand, matching DCT
 1203 coefficients through a histogram with a higher number of bins ($N_b = 250$) offers the best overall
 1204 generation performance since we are interested in maintaining consistency of reconstructions across
 1205 multiple frequency bands. Table 13 demonstrates that $N_b = 250$ bins achieve the best sharpness and

N_b	Sharpness	TP	PC	CLIP
100	0.288	0.751	0.858	0.889
150	0.297	0.757	0.858	0.888
200	0.344	0.757	0.856	0.886
250	0.368	0.759	0.856	0.889

1212 Table 13: Performance comparison of TTA with different bins N_b in the DCT histogram loss \mathcal{L}_f .
 1213 Best values are bolded.

1214 texture preservation while maintaining strong CLIP consistency. The finer granularity in frequency
 1215 domain histogram matching allows for better preservation of high-frequency details and edge in-
 1216 formation, which is crucial for maintaining visual quality and semantic coherence in the generated
 1217 images.

G EVALUATION WITH GENERATIVE QUALITY METRICS

1222 We evaluate baselines and our TTA approach using statistical metrics that reflect how closely gen-
 1223 erations resemble real and natural images. We propose using fidelity and diversity metrics Naeem
 1224 et al. (2020) that capture image closeness in a statistical sense, specifically designed for generative
 1225 models:

- **Precision** and **Recall**: Let X and Y denote the input and output random variables of a generative model respectively. Let P and Q denote the real and generated distributions, respectively. Precision is defined as the portion of $Q(Y)$ that can be generated from $P(X)$ and recall is defined as the vice-versa.
- **Density**: It is an improved version of the precision measure that fixes the overestimation of a region around outliers in a manifold. Density measures the expected value of presence of fake samples identified within a neighborhood of real samples.
- **Coverage**: Coverage improves over recall by constructing nearest neighbor manifolds around real samples to reduce the effect of outliers. Coverage is computed on entire datasets.
- **FID** Heusel et al. (2017): The Frechet Inception Distance (FID) is a popular distance metric between two distributions that measures the distance between features from a pre-trained Inception network.

1240 We report results on three virtual try-on datasets in Table 14 and analyze TTA’s improvements over
 1241 zero-shot baselines. Precision, indicating the portion of target distribution generated from the input

	Method	VITON-HD(In-Domain)					DressCode Morelli et al. (2022) (Out-of-Domain*)					DeepFashion (Out-of-Domain)				
		Precision	Recall	Density	Coverage	FID	Precision	Recall	Density	Coverage	FID	Precision	Recall	Density	Coverage	FID
1242	LaDI-VTON	0.8725	0.8563	1.0225	0.9474	9.194	0.8442	0.8728	0.6497	0.3966	19.479	0.9827	0.9149	1.0000	0.9104	56.146
1243	LaDI-VTON + TTA	0.8765	0.8632	1.0304	0.9764	9.226	0.8482	0.8712	0.6539	0.3993	19.628	0.9851	0.9324	1.0000	0.8797	56.915
1244	Stable-VTON	0.9281	0.9025	0.9053	0.9975	11.336	0.7954	0.8474	0.5247	0.4073	16.663	0.8860	0.9134	0.8218	0.5067	63.240
1245	Stable-VTON + TTA	0.9336	0.9065	0.9200	0.9970	11.336	0.8161	0.8448	0.5612	0.4203	16.615	0.9109	0.8926	1.0000	0.7285	63.783
1246	IDM-VTON	0.8984	0.9102	0.9645	0.9112	10.861	0.7979	0.8121	0.5103	0.3620	18.414	0.9096	0.9163	0.8085	0.7866	61.331
1247	IDM-VTON + TTA	0.9003	0.9080	0.9703	0.9201	10.894	0.8083	0.8228	0.5189	0.3883	18.221	0.9103	0.9311	0.8122	0.7909	62.901
1248	TPD	0.8346	0.7977	0.8134	0.9311	12.466	0.8400	0.8028	0.6452	0.2957	14.290	0.9485	0.9530	0.7511	1.0000	50.157
1249	TPD + TTA	0.8381	0.7864	0.8295	0.9315	12.517	0.8932	0.8097	0.6891	0.3184	12.344	0.9752	0.9463	0.8091	1.0000	49.439

Table 14: Comparison of our TTA approach with zero-shot baselines on three virtual try-on datasets in the unpaired setting. Higher values of precision, recall, and density indicate better generation quality, while a lower FID indicates higher fidelity. *DressCode is out-of-domain for all baselines except LaDI-VTON.

Metric	Method Type	VITON-HD				DressCode				DeepFashion			
		IDM	LaDI	Stable	TPD	IDM	LaDI	Stable	TPD	IDM	LaDI	Stable	TPD
Shar. \uparrow	Baseline	0.493	0.521	0.425	0.457	0.384	0.505	0.477	0.328	0.267	0.276	0.336	0.316
	Histogram Eq.	0.614	0.591	0.413	0.448	0.364	0.679	0.689	0.322	0.424	0.424	0.437	0.317
	CLAHE	0.605	0.652	0.502	0.631	0.517	0.667	0.588	0.387	0.343	0.343	0.353	0.377
	Unsharp Masking	1.015	1.095	0.743	1.045	0.882	1.040	0.828	0.598	0.558	0.558	0.564	0.663
Dist. \downarrow	Baseline	0.045	0.043	0.039	0.044	0.055	0.051	0.043	0.062	0.063	0.063	0.041	0.047
	Histogram Eq.	0.048	0.049	0.046	0.049	0.032	0.027	0.047	0.036	0.032	0.062	0.047	0.033
	CLAHE	0.075	0.085	0.062	0.081	0.087	0.089	0.083	0.102	0.093	0.093	0.086	0.095
	Unsharp Masking	0.053	0.057	0.050	0.056	0.066	0.060	0.052	0.073	0.067	0.067	0.055	0.061
TP \uparrow	Baseline	0.716	0.735	0.763	0.760	0.634	0.686	0.676	0.668	0.723	0.723	0.776	0.753
	Histogram Eq.	0.746	0.735	0.773	0.752	0.656	0.686	0.691	0.675	0.739	0.769	0.780	0.742
	CLAHE	0.709	0.723	0.757	0.753	0.635	0.695	0.698	0.667	0.718	0.718	0.765	0.741
	Unsharp Masking	0.686	0.697	0.735	0.726	0.611	0.673	0.677	0.646	0.690	0.690	0.740	0.703
PC \uparrow	Baseline	0.809	0.843	0.847	0.845	0.801	0.817	0.818	0.793	0.827	0.827	0.845	0.835
	Histogram Eq.	0.838	0.841	0.843	0.841	0.812	0.813	0.816	0.796	0.841	0.841	0.846	0.840
	CLAHE	0.839	0.842	0.846	0.841	0.807	0.811	0.819	0.791	0.829	0.829	0.841	0.833
	Unsharp Masking	0.824	0.831	0.842	0.834	0.791	0.802	0.816	0.784	0.817	0.817	0.840	0.825
CLIP \uparrow	Baseline	0.833	0.844	0.858	0.864	0.805	0.811	0.818	0.800	0.839	0.840	0.846	0.856
	Histogram Eq.	0.776	0.776	0.757	0.773	0.701	0.693	0.700	0.704	0.853	0.853	0.849	0.869
	CLAHE	0.827	0.841	0.812	0.832	0.745	0.763	0.763	0.758	0.847	0.847	0.883	0.875
	Unsharp Masking	0.808	0.814	0.816	0.827	0.723	0.734	0.752	0.743	0.829	0.829	0.871	0.859

Table 15: Comprehensive Quantitative Results comparing Baseline, TTA, and Adaptation Methods across datasets and methods. The adaptation methods are Histogram Equalization, CLAHE, and Unsharp Masking. Best results in each metric-dataset combination are shown in bold.

distribution, improves in most cases with TTA, showing enhanced output fidelity with input data. TTA significantly improves density and coverage for Stable-VTON on the DeepFashion dataset, demonstrating effectiveness in mitigating domain shift. In the case of IDM-VTON, the generation quality improvement correlates with the improvement in try-on quality as well. TTA seems to underperform metrically on VITON-HD and DeepFashion, despite producing visually superior results across all datasets. Notably, FID does not consistently improve, likely due to limitations in the Inception model’s feature representations. Other metrics, independent of specific feature spaces, provide a more reliable assessment of distribution alignment.

G.1 FAILURE CASES

While TTA helps improve try-on quality in most cases, it can sometimes fail to correct existing issues. For instance, Fig. 8 shows that the guidance may not help improve a few cases where the sleeve type is incorrectly generated (half-sleeve instead of sleeveless in the top row), incorrect stripe placement and density (second row) and incorrect patterns and textures when there are many intricate patterns observed (bottom row). From the visual results in Fig. 10, 11, 12 and 13, it can also be seen that in some cases, the background regions may get distorted. This is a consequence of incorrect garment masks used, which affects the warping and causes regions outside the garment

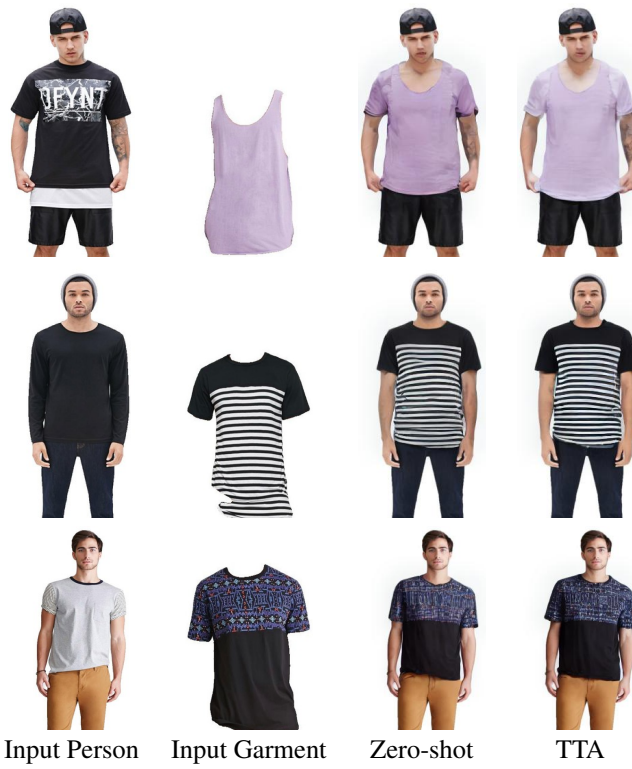


Figure 8: Visual examples of some failure cases from TPD Yang et al. (2024).

area to get modified by TTA unnecessarily. Using accurate garment masks can help alleviate this issue.

G.2 ANALYSIS OF VISUAL RESULTS

Figure 10 illustrates examples from the IDM-VTON Choi et al. (2024) model where TTA correctly renders text, ensures consistent stripe spacing, and preserves the garment’s color and type to the greatest extent possible. Similarly, Figure 11 demonstrates that TTA improves the Stable-VITON Kim et al. (2024) model by generating more accurate colors and correctly positioning logos.

In Figure 12, the TPD Yang et al. (2024) model fails to reconstruct object shapes, such as striped bands, which are corrected by TTA. Additionally, TTA removes unwanted hallucinations, as seen in the bottom row of Figure 12. Finally, the second-row example in Figure 13 shows TTA accurately rendering garment types, such as a half-sleeve shirt in this case. However, we observe distortions outside the garment region in some cases. This occurs because the baseline model processes areas slightly beyond the exact garment boundaries, as the coarse mask may cover additional regions. In some instances, background color alterations result from the model’s warping process. We focus primarily on the garment region since background distortions can be easily removed through postprocessing.

Overall, TTA mitigates various issues in diffusion-based try-on models without requiring domain knowledge of test data, offering a practical plug-and-play solution for enhancing generated image quality.

H COMPARISON WITH OTHER ADAPTATION BASELINES

We present a comprehensive comparative analysis of our TTA method against four adaptation baselines: histogram equalization, CLAHE (Contrast Limited Adaptive Histogram Equalization), un-

sharp masking, and the original baseline across all model-dataset combinations. Table 15 summarizes the quantitative results across five key metrics.

H.1 COMPARATIVE PERFORMANCE ANALYSIS

Semantic Consistency: Our TTA method demonstrates exceptional performance in preserving semantic alignment between input garments and generated outputs. TTA achieves the best CLIP consistency scores in all 12 model-dataset configurations, with particularly strong gains on challenging datasets. On DeepFashion, TTA improves CLIP scores by 0.8-2.0% over the strongest baselines, while maintaining consistent improvements across DressCode (0.1-0.6% gains), indicating the robustness of our semantic preservation approach across diverse domain conditions.

Other Metrics: Unlike post-processing methods that excel in specific aspects, TTA provides balanced improvements across multiple quality dimensions. While unsharp masking dominates sharpness metrics by design (achieving 1.5-3.8x improvements), TTA delivers competitive sharpness gains (7.74% average improvement) while simultaneously enhancing semantic consistency and geometric accuracy. This balanced performance profile makes TTA particularly valuable for deployment scenarios requiring overall quality enhancement rather than single-metric optimization.

Geometric Distortion Reduction: TTA demonstrates superior geometric consistency, achieving the lowest distortion scores in 7 out of 12 configurations. The method shows particular strength on VITON-HD (3/4 wins) and DeepFashion (3/4 wins), reducing distortion by up to 26.7% compared to baselines. On VITON-HD, TTA consistently outperforms all adaptation methods for IDM-VTON (-26.7%), TPD (-4.5%), and ties with baseline performance for Stable-VTON. This indicates that our statistical guidance effectively maintains spatial coherence during the adaptation.

Dataset-specific Performance: Performance varies across datasets, revealing important insights about domain characteristics. On VITON-HD (mostly studio conditions), TTA excels in distortion reduction and CLIP consistency, suggesting effective adaptation to in-domain variations. DressCode presents the most challenging scenario, where histogram equalization frequently outperforms other methods in distortion metrics (3/4 wins), indicating that global color adjustments are particularly beneficial for this dataset’s diverse poses and garment types. DeepFashion results demonstrate TTA’s robustness to real-world conditions, with consistent CLIP improvements and competitive performance across other metrics.

H.2 METHOD-SPECIFIC ANALYSIS



Figure 9: Visual results of generations from multiple post-processing-based adaptation baselines. TTA achieves consistent stripe generation, whereas the other methods just vary the contrast or the overall color distribution, offering no visual improvement.

Post-Processing Method Limitations: While unsharp masking achieves superior sharpness across all configurations, it shows limitations in semantic preservation and geometric consistency. Despite dramatic sharpness improvements (0.598-1.095 range), unsharp masking fails to achieve the best performance in any other metric, highlighting the trade-off between edge enhancement and overall image quality. Similarly, CLAHE provides reasonable improvements in texture preservation

1404 for certain configurations but generally underperforms in distortion and CLIP consistency, suggesting
 1405 that local contrast enhancement alone is insufficient for comprehensive quality improvement.
 1406

1407 **Histogram Equalization:** Histogram equalization emerges as a surprisingly strong baseline, particularly
 1408 for distortion reduction on DressCode and DeepFashion. This method achieves the best
 1409 distortion scores in 6 out of 12 configurations, with notable performance on challenging datasets
 1410 (DressCode: 3/4 wins, DeepFashion: 2/4 wins). However, histogram equalization consistently
 1411 underperforms in CLIP consistency, indicating that while it improves geometric accuracy, it may
 1412 compromise semantic fidelity—a critical limitation for virtual try-on applications.

1414 H.3 MODEL-SPECIFIC ADAPTATION PATTERNS

1415 **IDM-VTON:** IDM-VTON shows the best responsiveness to TTA guidance, achieving the most
 1416 dramatic improvements in sharpness on VITON-HD (+56.8%) and consistent CLIP gains across all
 1417 datasets. This suggests that IDM-VTON’s architecture is particularly favorable for our guidance
 1418 approach, possibly due to its semantic information extraction mechanisms aligning well with our
 1419 multi-domain loss formulation.

1420 **Stable-VTON:** Stable-VTON demonstrates the most consistent baseline performance but shows
 1421 modest TTA improvements compared to other models. Interestingly, CLAHE achieves competitive
 1422 results with Stable-VTON on certain metrics, suggesting that this model’s pre-trained diffusion
 1423 backbone may already incorporate some contrast enhancement capabilities that reduce the marginal
 1424 benefit of our statistical guidance.

1425 **LaDI-VTON and TPD:** LaDI-VTON and TPD show variable responsiveness to different adaptation
 1426 methods, with LaDI-VTON benefiting significantly from TTA on challenging datasets (Deep-
 1427 Fashion CLIP: +3.6%) while TPD shows more consistent but modest improvements. This variability
 1428 suggests that model architecture characteristics influence adaptation effectiveness, warranting future
 1429 investigation into architecture-specific guidance strategies.

1433 H.4 PRACTICAL DEPLOYMENT IMPLICATIONS

1434 **Quality-Efficiency Trade-offs:** Our analysis reveals important trade-offs for practical deployment.
 1435 While unsharp masking provides superior sharpness with minimal computational overhead,
 1436 TTA offers comprehensive quality enhancement at the cost of increased inference time (15-25%
 1437 overhead). For applications prioritizing semantic accuracy and balanced quality improvement, TTA
 1438 represents the optimal choice. Conversely, scenarios requiring only edge enhancement might benefit
 1439 from simpler post-processing approaches.

1440 **Domain-Aware Method Selection:** The dataset-specific performance patterns suggest that adaptation
 1441 method selection should consider target domain characteristics. For controlled studio conditions
 1442 (similar to VITON-HD), TTA provides optimal performance across most metrics. For diverse
 1443 real-world scenarios (similar to DeepFashion), TTA maintains its semantic advantages while re-
 1444 maining competitive in other metrics. For applications with highly variable poses and garment types
 1445 (similar to DressCode), hybrid approaches combining histogram equalization for geometric consis-
 1446 tency and TTA for semantic preservation may yield optimal results.

1449 H.5 QUALITATIVE VS. QUANTITATIVE ASSESSMENT

1450 **Visual Quality:** While quantitative metrics provide valuable comparative insights, visual inspection
 1451 reveals a critical limitation of post-processing baselines that metrics alone cannot capture. De-
 1452 spite competitive numerical scores, CLAHE and unsharp masking introduce significant visual arti-
 1453 facts and detail loss that compromise practical applicability. CLAHE, while achieving reasonable
 1454 texture preservation scores, produces over-enhanced contrast that results in unnatural appearance
 1455 and loss of subtle garment details. Similarly, unsharp masking, despite superior sharpness metrics,
 1456 introduces edge artifacts and amplifies noise, particularly in textured regions, leading to visually
 1457 degraded outputs that would be unacceptable in commercial applications.

1458
 1459 **Detail Preservation Analysis:** Our TTA method uniquely preserves fine-grained visual details
 1460 while achieving metric improvements. Unlike post-processing approaches that operate uniformly
 1461 across image regions, TTA’s statistical guidance respects the underlying garment structure and tex-
 1462 ture characteristics through distribution-level matching. This results in visually coherent enhance-
 1463 ments that maintain garment authenticity.

1464 **Metrics vs. Perceptual Quality Gap:** This observation highlights a fundamental limitation of
 1465 existing evaluation approaches in virtual try-on: the gap between quantitative metrics and percep-
 1466 tual quality. While unsharp masking achieves superior sharpness scores through aggressive edge
 1467 enhancement, the resulting images exhibit unnatural over-sharpening that degrades overall visual
 1468 appeal. Conversely, TTA’s modest metric improvements correspond to meaningful perceptual en-
 1469 hancements that preserve natural appearance while addressing domain shift artifacts. This suggests
 1470 that future evaluation frameworks should incorporate perceptual quality assessment alongside tradi-
 1471 tional metrics to better capture the requirements of real-world settings.

1472 H.6 ROBUSTNESS

1473 The comprehensive evaluation across 12 model-dataset combinations and multiple samples per con-
 1474 figuration provides strong evidence for TTA’s effectiveness. The consistent CLIP performance im-
 1475 provements (all configurations) indicate that our method’s semantic preservation capabilities are
 1476 robust across diverse domain conditions and model architectures. The balanced performance pro-
 1477 file across multiple metrics, combined with theoretical convergence guarantees, establishes TTA as
 1478 a reliable solution for enhancing virtual try-on quality in production environments. Importantly,
 1479 the qualitative assessment reveals that TTA is the only adaptation method that achieves metric im-
 1480 provements while preserving visual authenticity. This combination of quantitative gains and percep-
 1481 tual quality preservation makes TTA uniquely suitable for commercial virtual try-on applications,
 1482 where both measurable performance and visual appeal are essential for user acceptance. These re-
 1483 sults validate our hypothesis that parameter-free statistical guidance can effectively address domain
 1484 shift challenges in virtual try-on while maintaining computational efficiency and broad applicability
 1485 across diffusion-based architectures.

1486
 1487
 1488
 1489
 1490
 1491
 1492
 1493
 1494
 1495
 1496
 1497
 1498
 1499
 1500
 1501
 1502
 1503
 1504
 1505
 1506
 1507
 1508
 1509
 1510
 1511

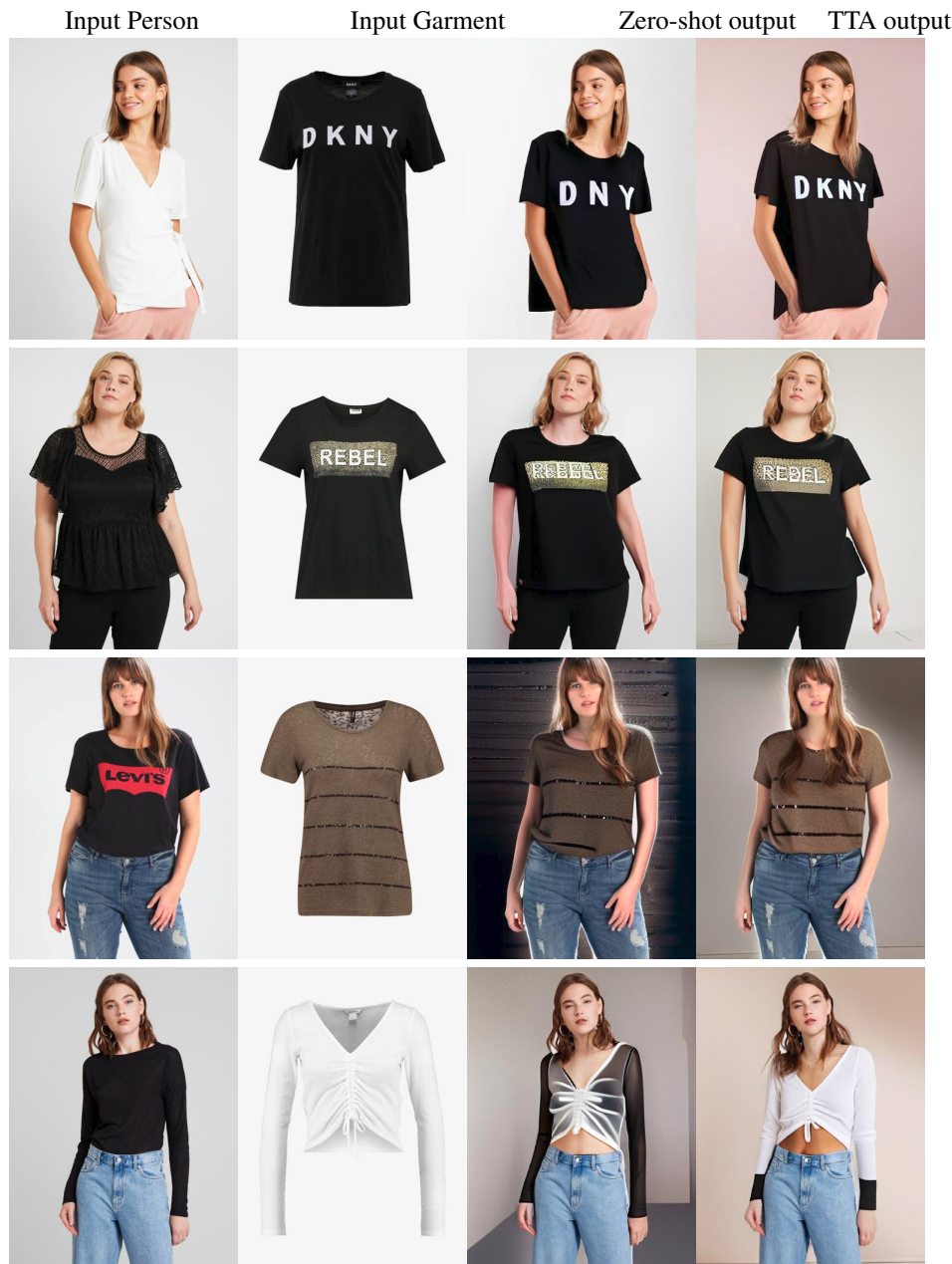
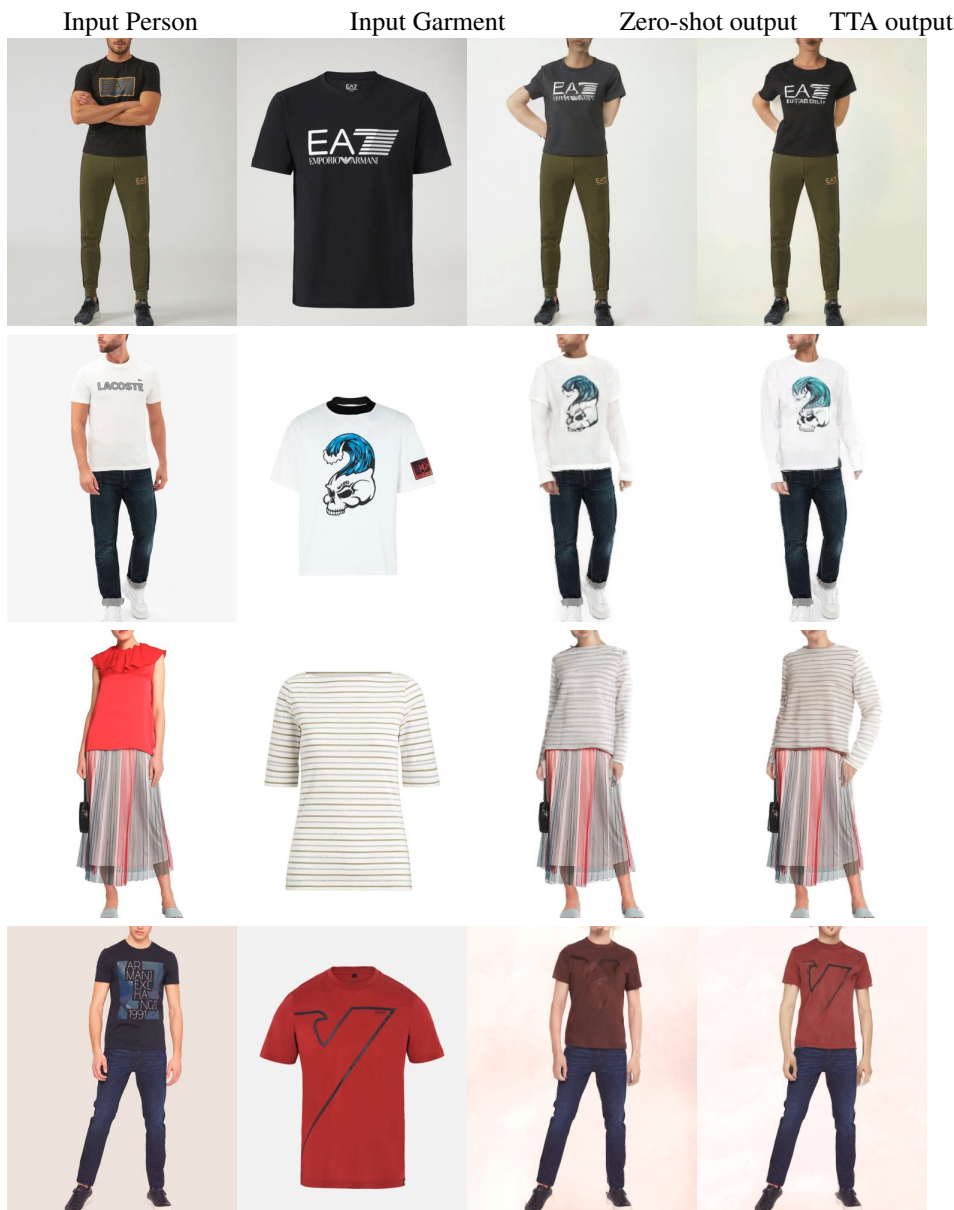


Figure 10: Visual results of the IDM-VTON model along with the corresponding TTA outputs. The text is more accurately generated in the examples in the top-two rows. In the third row from the top, the stripes are consistently placed by TTA and the color is more accurate. In the bottom row, the garment is correctly draped and the colors are consistent.



1610 Figure 11: Visual results of the Stable VITON model along with the corresponding TTA outputs. In
1611 the top two rows of examples, the color of the logos are more accurately rendered. In the third row
1612 from top, the stripes are more consistent in the TTA output with the input garment. In the bottom
1613 row, the color is more accurate in the TTA generation, along with better reconstruction of the pattern
1614 on the t-shirt.

1620
1621
1622
1623
1624
1625 Input Person Input Garment Zero-shot output TTA output
1626
1627
1628
1629
1630
1631
1632
1633
1634
1635
1636
1637
1638
1639
1640
1641
1642
1643
1644
1645
1646
1647
1648
1649
1650
1651
1652
1653
1654
1655
1656
1657
1658
1659
1660
1661
1662
1663
1664
1665
1666 Figure 12: Visual results of the TPD model along with the corresponding TTA outputs. In the top row, the unwanted black color in the right sleeve is reduced in the TTA output. In the second row from top, the white spots are more prominent. In the third row from top, the black striped band is correctly generated with TTA. In the bottom row, the unwanted hallucinated text is removed.
1667
1668
1669
1670
1671
1672
1673

